

# Investigation of Laser-Induced-Liquid- Beam-Ion-Desorption (LILBID) with Molecular Dynamics Simulations

Dissertation  
for the award of the degree  
“Doktor der Naturwissenschaften” (Dr. rer. nat.)  
Division of Mathematics and Natural Sciences  
of the Georg-August-Universität Göttingen

submitted by  
**Frank Wiederschein**

from Peine  
Göttingen 2009

Thesis Committee:

Prof. Dr. Helmut Grubmüller (Reviewer)

Prof. Dr. Bernd Abel (Reviewer)

Prof. Dr. Marcus Müller

Date of the oral examination:

## Affidavit

Frank Wiederschein  
Bühlstrasse 9  
37073 Göttingen

Hiermit erkläre ich an Eides statt, dass ich die vorliegende Dissertation mit dem Thema “Investigation of Laser-Induced-Liquid-Beam-Ion-Desorption (LIL-BID) with Molecular Dynamics Simulations” selbstständig und ohne unerlaubte Hilfe verfasst habe.

Göttingen, 30.11.2009



# Contents

<b>1</b>	<b>Introduction</b>	<b>1</b>
<b>2</b>	<b>Theory and Concepts</b>	<b>5</b>
2.1	Molecular Dynamics . . . . .	5
2.1.1	The Born-Oppenheimer Approximation . . . . .	6
2.1.2	Force Fields . . . . .	7
2.1.3	Classical Dynamics . . . . .	8
2.2	Monte Carlo Simulations . . . . .	8
2.3	Principle Component Analysis . . . . .	9
<b>3</b>	<b>Hemoglobin Desorption</b>	<b>11</b>
3.1	Methods . . . . .	11
3.1.1	Experimental Setup . . . . .	12
3.1.2	MD Setup . . . . .	13
3.2	Results & Discussion . . . . .	19
3.2.1	Shock Wave . . . . .	19
3.2.2	Ablation Process . . . . .	21
3.2.3	Hemoglobin Stability . . . . .	25
3.3	Conclusions . . . . .	29
<b>4</b>	<b>Charge Mechanism of Droplets</b>	<b>31</b>
4.1	Experiment . . . . .	31
4.2	Methods . . . . .	33
4.2.1	Statistical Model . . . . .	33
4.2.2	Interacting Model . . . . .	33
4.2.3	Dynamical Model . . . . .	35
4.3	Results & Discussion . . . . .	35
4.4	Conclusion . . . . .	42
<b>5</b>	<b>Summary &amp; Conclusion</b>	<b>45</b>

6

*CONTENTS*

**6 Appendix**

**49**

# Chapter 1

## Introduction

Mass Spectrometry (MS) is an analytical technique to determine the elemental composition of a sample. The sample can be a simple gas phase like the atmosphere on Earth or Mars. But it is also possible to analyze liquids as complex as blood or urine and even the characterization of biomolecule complexes is possible. For all of them, the basic principles of MS are the same. The first step is the ionization of the sample compounds to generate charged molecules and then obtain their mass-to-charge ratios. The ionization process of chemical compounds can be quite simple in the case of gas phase molecules or very challenging in the case of fragile oligomeric biomolecules in solution like hemoglobin.

The most popular MS methods to analyze biomolecules are Electrospray Ionization (ESI) and Matrix-Assisted Laser Desorption/Ionization (MALDI).

ESI is the method of choice, when the interaction between non-covalently bound molecules is of interest or when the MS should be coupled with liquid chromatography. The basic concepts of ESI is to disperse a liquid, containing the analyte, into a charged fine aerosol. The droplets of this aerosol undergo a cycle of evaporations and coulomb explosions until the charged analyte is liberated into the gas phase. From there on, the mass-to-charge ratio can be obtained by a Time-Of-Flight (TOF) MS. The dispersed liquid consists primarily of water, some volatile organic compounds and an analyte. The volatile compounds reduce the initial droplet size of the aerosol and increase the conductivity of the liquid. This is very important for the dispersion, which is achieved by guiding the fluid through a highly charged metallic capillary. At the tip of the capillary a Taylor cone is formed, which emits a thin jet through its apex. The jet breaks into small charged droplets. These droplets shrink by evaporation until their sizes reach the Rayleigh limit. From that point on onward, they become unstable and emit jets, which carry large

percentages of the initial droplet charges. This circle of evaporation and Rayleigh fission takes place until the analyte carrying most of the charge of the droplet is liberated into gas phase. The larger the molecules investigated by ESI are, the higher are the charge states, these molecules can achieve during the process of ionization. Overall this process is quite soft, meaning that even large covalently bound complexes can be detected with little fragmentation of the analyte.

MALDI is similar to ESI in softness, but the ionization mechanism is completely different. The analyte forms a crystal with a matrix consistent of acids, organic solvents and highly purified water. This crystal is then irradiated with an UV nitrogen laser, which leads to the ionization of the analyte. The matrix has to absorb the laser irradiation very efficiently to protect the analyte from being destroyed and also has to support the evaporation and ionization of the analyte. The ions are emitted individually (desorption) at low laser fluences or at high fluence even larger clusters are emitted from the crystal (ablation) [25]. The latter process is dominated by laser-induced shock waves in the matrix [14]. The resulting ions in gas phase are less charged, than the ions produced by ESI. Even single charged molecules are detected with a TOF MS.

Both ionization methods are soft and have their advantages. The major strength of ESI is its liquid phase matrix, whereas MALDI has the advantage to cover a large analyte to matrix concentration range. But none of them is able to provide a physiological environment for the analyte, nor allow a quantitative analysis. Recently, a new ionization technique (Laser-Induced-Liquid-Beam-Ion-Desorption), (LILBID) has been developed, which is able to overcome this shortcoming [24, 6]. LILBID is a very soft ionization method, even compared to ESI or MALDI [36, 21]. Even non-covalently bound complexes like the tetrameric hemoglobin can be ionized without fragmentation by the LILBID method. Before LILBID, this was only achieved by ESI [27, 8]. To mention is the distinct distribution of charge states of the ionized analyte. MALDI and especially ESI have the tendency to higher charge states, whereas LILBID on the other hand results in low, mostly single charge states of the analyte.

The basic concept of LILBID is shown in Figure 1.1. A sharp IR laser pulse tuned on the HO stretch vibration of bulk water irradiates the surface of a thin water beam, which leads to the ionization of the solvated analyte. The strong ultra fast heating of the water beam surface not only causes direct desorption of matrix and analyte molecules, but also induces strong shock



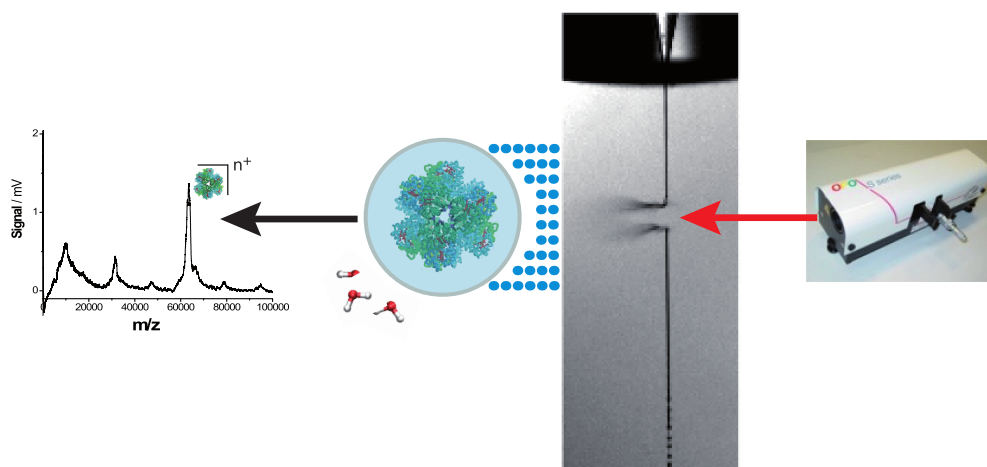


Figure 1.1: LILBID scheme. A 7 ns Laser pulse, which is tuned on the HO-stretch vibration of bulk water, heats up a water beam. This leads to an ablation of water droplets containing molecules, which are detected by a Time-Of-Flight mass spectrometer.

waves, which propagate through the water beam, resulting in an anisotropic explosion of the water beam [6]. The shock wave-induced ablation of droplets from the water jet is most likely the ionization pathway, which is responsible for the remarkable softness of the LILBID method, because the conditions in the high energy environment of the direct desorption area are too rough. But up to date there are no studies available which elucidate the process of LILBID ionization, like there are for ESI or MALDI [14], testing this hypothesis.

Due to the fact, that the ionization process of MALDI is quite similar to the one of LILBID (both are laser-induced and feature shock wave-induced ablation), methods which helped to investigate the ionization process of MALDI might also be useful to shed light on the ionization process of LILBID. One of the most helpful method to investigate the mechanism of MALDI on atomistic level is Molecular Dynamics (MD) simulations [25, 13, 37, 16, 17]. In this work MD simulations will be used to investigate the shock wave-induced ablation of solvated molecules. In particular, the following questions will be addressed. First, it will be investigated why the ablation process leaves the non-covalently bound molecule complexes intact despite the high temperature and pressure, which occur during the passage of the shock wave (chapter 3). Second, the question will be addressed how the analyte loses its water shell after the ablation. To answer this question the temperature of the ablated droplet for possible evaporation pathways and the charge state

of the droplet are of main interest. And third, close to the second question, I will work on an explanation for the observed charge distribution. To answer the last question not only MD simulation has been performed, but also gedankenexperiments based on the statistical concept of the Poisson distribution and Monte Carlo (MC) simulations have been performed in chapter 4.

# Chapter 2

## Theory and Concepts

This chapter outlines the general theoretical framework of this thesis and the basics of the applied methods. First classic Molecular Dynamics Simulations will be introduced. Second the Metropolis Monte Carlo method will be described. And finally the Principle Component Analysis (PCA), i.e., a powerful method to analyse the dynamic behavior of Molecular Dynamics Simulations will be briefly described. Details on the particular method and detailed setups are given in the respective chapters.

### 2.1 Molecular Dynamics

The simulation method used in this thesis has to meet two different demands. First it has to have the ability to describe the time evolution of molecular systems in atomistic detail to reproduce their structure and physical properties under normal conditions (pressure, temperature). Second the simulation method of choice has to reproduce the influence of a strong shock wave on such a molecular system, leading to extreme conditions. MD was invented with the intension to cope with the first point and is therefore a sufficient method for this demand. In 1980 Holian showed [23, 22], that MD simulations are also appropriate to describe the propagation of shock waves to an equal accuracy as analytical solutions of the Mott-Smith model [30] or other simulation methods like numerical solutions of the Navier-Stocks equations. Therefore, Molecular Dynamics will be used as the simulation method of choice in this thesis.

To give an overview of MD simulations, three main approximations will be briefly described, which are necessary to reduce to computational effort of evaluating a molecular system in time to a feasible amount. These are first, the decoupling of nuclear and electronic motions (Born-Oppenheimer Ap-

proximation), second, the use of an empirical force field to describe the interactions between particles, and third, the classical description of the nuclei motion (Classical Dynamics). For a comprehensive description of the MD simulation techniques we refer the reader to the review of Gunsteren [34]; a more detailed account is given in the textbook of Leach [26].

### 2.1.1 The Born-Oppenheimer Approximation

The evolution in time of any molecular system is described by the time-dependent Schrödinger equation,

$$\hat{H}\psi = i\hbar\frac{\partial\psi}{\partial t}, \quad (2.1)$$

where  $\hat{H}$  is the Hamilton operator, i.e., the sum of the kinetic and potential energy,  $\psi$  is the wave function, involving the coordinates of both nuclei and electrons, and  $\hbar = h/2\pi$  with  $h$  Planck's constant. The general idea behind the Born-Oppenheimer Approximation is to decouple the motion of the electrons from that of the nuclei. Due to the much lower mass of the electrons, and, consequently, the much higher velocity of the electrons compared to the nuclei, the electronic wave function can be assumed to instantaneously follow the nuclei motion. This assumption leads to a separation of the wave function into an electronic part  $\psi_e$  and a nuclear part  $\psi_n$ ,

$$\psi(\mathbf{r}, \mathbf{R}) = \psi_n(\mathbf{R})\psi_e(\mathbf{r}; \mathbf{R}), \quad (2.2)$$

where  $\mathbf{R}$  denotes the coordinates of the nuclei and  $\mathbf{r}$  the coordinates of the electrons. The nuclei are then moving on a potential energy surface (PES)  $E_e$  created by the electronic Hamiltonian  $\hat{H}_e$ . The time-independent Schrödinger equation of the electrons makes the nuclei motion on the PES approachable,

$$\hat{H}_e\psi_e = E_e\psi_e, \quad (2.3)$$

The nuclei coordinates appear in the electronic Hamiltonian as parameters. Solving the time-independent Schrödinger equation (Eq. 2.3) of the electrons for different nuclei coordinates  $\mathbf{R}$  leads to dependency of the PES  $E_e$  from the nuclei coordinates. The Born-Oppenheimer Approximation reduces the computational effort to describe the time evolution of the system enormously, by reducing the degrees of freedom drastically.

### 2.1.2 Force Fields

Even by taking advantage of the Born-Oppenheimer Approximation to evaluate the potential energy  $E_e$  of the system by solving the electronic Schrödinger equation (Eq. 2.3), this approach is computationally much too expensive to evolve a large molecular system in time, as required in this thesis. Therefore, a second approximation is necessary to reduce the computational effort of calculating the PES. The PES  $E_e$  will be approximated by a sum of analytical functions  $V(\mathbf{R})$  (Eq. 2.4),

$$\begin{aligned}
 E_e(\mathbf{R}) \approx V(\mathbf{R}) = & \sum_{\text{bonds } i} V_b^i + \sum_{\text{angles } j} V_a^j + \sum_{\text{impropers } k} V_{imp}^k \\
 & + \sum_{\text{dihedrals } l} V_d^l + \sum_{\text{pairs } n,m} V_{\text{Coul}}^{n,m} + \sum_{\text{pairs } n,m} V_{\text{LJ}}^{n,m}.
 \end{aligned} \tag{2.4}$$

This sum is called the molecular mechanical (MM) force field of the system. In general, the sum consist of two types of interactions. First, four bonded terms, of which  $V_b$ ,  $V_a$  and  $V_{imp}$  are harmonic functions and only  $V_d$  is a cosine function. Exceptionally, in the case of the GROMOS96 43A1 force field [11], one of the force fields used in this thesis, the angle term  $V_a$  also is a cosine function. Second, two terms  $V_{\text{LJ}}$  and  $V_{\text{Coul}}$ , which describe the non-bonded interactions of the system. The Lennard-Jones term  $V_{\text{LJ}}$  represents the Van-der-Waals attraction and the Pauli repulsion. The Coulomb term  $V_{\text{Coul}}$  describes the electrostatic interaction. The non-bonded terms are calculated pairwise. In principle, all atom pairs should be included, but the neighbour non-bonded interactions are already taken into account implicitly by the bonded terms. Therefore only a subset of the atom pairs is taken into account. For a comprehensive description of all force field terms in detail, see the article of Oostenbrink about the GROMOS96 53A5/53A6 force field [31], which is also used in this thesis. The parameters for all GROMOS96 force fields are derived by reproducing thermodynamic properties, primarily the free enthalpies of hydration and apolar solvation of a wide range of compounds. The aliphatic carbons and the bonded hydrogens ( $\text{CH}_1$ ,  $\text{CH}_2$ ,  $\text{CH}_3$ ,  $\text{CH}_4$ ) are treated as united atoms by the GROMOS96 force field. This united-atom approach yields a massive reduction of the degrees of freedom, which may reduce the computational effort to compute the potential energy up to a factor of nine.

### 2.1.3 Classical Dynamics

The time evolution of large biomolecular systems is not feasible by solving the time-dependent Schrödinger equation quantum mechanically even with the two mentioned approximations. To further reduce the computational cost of describing the nuclear dynamics, a third approximation is necessary, which is the classical description of the nuclei dynamics by Newton's second law,

$$-\nabla_i V(\mathbf{R}) = \mathbf{F}_i = m_i \mathbf{a}_i = m_i \frac{d^2 \mathbf{R}_i(t)}{dt^2}, \quad (2.5)$$

where  $V(\mathbf{R})$  is the potential energy, described by the force field, and  $\mathbf{R}_i$ ,  $m_i$  and  $\mathbf{a}_i$  are the coordinates, mass and acceleration of atom  $i$ , respectively. The force  $\mathbf{F}_i$  acting on atom  $i$  leads to a change of velocity of this atom. Thus the integration of equation 2.5 is the basic of any MD code to generate the trajectory of the system. In this work, the leap-frog algorithm (Eq. 2.6) will be used to integrate Newton's equation of motion,

$$\begin{aligned} \mathbf{R}_{(t+\Delta t)} &= \mathbf{R}_{(t)} + \mathbf{v}_{(t+\frac{1}{2}\Delta t)}\Delta t \\ \mathbf{v}_{(t+\frac{1}{2}\Delta t)} &= \mathbf{v}_{(t-\frac{1}{2}\Delta t)} + \mathbf{a}_{(t)}\Delta t. \end{aligned} \quad (2.6)$$

The leap-frog algorithm is a modification of the velocity Verlet algorithm [35] with identical properties. The algorithm is a second order method to integrate differential equations and is exceptionally stable, i.e., guaranties energy conservation of the whole system, as long as the width of the integration time step  $\Delta t$  is much shorter than the fastest oscillation of the system. Bound vibrations of covalently bounded hydrogens are the fastest motions occurring in a molecular system. This leads to a time step  $\Delta t$  of  $\approx 1$  fs.

## 2.2 Monte Carlo Simulations

If the dynamics of a system are not of interest, then there are more efficient methods available to sample the configuration space of a system than MD simulations. The Monte Carlo (MC) approach samples only the PES of a system and therefore is faster than MD simulations, because the MC method only needs to calculate the potential energy of a given conformation, instead of calculating the forces, acting on the atoms in the system. To reproduce the distribution of interacting ions in a water box (chapter 4) the Metropolis MC algorithm will be used as proposed 1953 by Metropolis [28]. The interactions between water and ions will be taken into account implicitly by the relative static permittivity  $\epsilon_r = 80$  of water, in order to heavily reduce the

effort of computing the potential energy  $E(\mathbf{R})$  of the system.

A short description of the necessary steps of the Metropolis MC method follows. First the potential energy  $E(\mathbf{R})$  (Eq. 2.7) of the system is calculated. In the system investigated in chapter 4, only the Coulomb interaction between the ions contributes to the potential energy  $E(\mathbf{R})$ ,

$$E(\mathbf{R}) \approx E_{\text{Coul}}(\mathbf{R}) = \frac{1}{4\pi\epsilon_0\epsilon_r} \sum_{i,j,i \neq j}^N \frac{q_i q_j}{R_{ij}}, \quad (2.7)$$

where  $q_i, q_j$  denote ion charges,  $R_{ij}$  are their mutual distances,  $\epsilon_0$  is the electric constant and  $\epsilon_r$  is the relative static permittivity.

During one MC step, one randomly chosen atom is placed within a certain distance to new randomly chosen position. The potential energy of this new conformation is compared to that of the former conformation. If the energy of the new conformation is lower than the former, the MC step is accepted. If the energy of the new conformation is higher, then the MC step is also accepted with a probability of  $\exp(-(E_{\text{new}} - E_{\text{old}})/k_B T)$  ( $k_B$  is the Boltzmann constant and  $T$  is the system temperature), and otherwise rejected. By accepting steps, which lead to higher energies, the method is able to pass energy barriers and escape local minima. This algorithm is ergodic and allows that the ensemble approaches the canonical distribution, if a sufficient amount of MC steps have been performed and if the system itself is ergodic.

## 2.3 Principle Component Analysis

The Principle Component Analysis is a powerful method to study the dynamics of a molecular systems. In chapter 3 PCA is used to investigate the dynamics of hemoglobin under the influence of a strong transient shock wave. Even in large and complex molecules such as hemoglobin only a few essential degrees of freedom describe the internal motion sufficient. One method to separate these essential degrees of freedom from the majority of less important degrees of freedom is Principle Component Analysis [2, 19]. Therefore the covariance matrix  $C_{ij}$  (Eq. 2.8) of the atomic displacement is diagonalized, to transform correlated Cartesian coordinates of selected atoms to an uncorrelated set of principal components, e.g., in chapter 3 the PCA is performed on the backbone atoms of hemoglobin. This transformation is a rotation that aligns the transformed axes (principal components) with the

directions of maximum variance,

$$\begin{aligned} C_{ij} &= \langle (x_i - \langle x_i \rangle) (x_j - \langle x_j \rangle) \rangle, \\ C &= R \text{diag}(\lambda_1, \lambda_2, \dots, \lambda_{3N}) R^T, \end{aligned} \tag{2.8}$$

where  $x_i$  are Cartesian coordinates of the atom of interest and  $R$  denotes the rotation matrix, which consists of the eigenvectors or principal components corresponding to the eigenvalues  $\lambda_i$  of  $C$ . The eigenvalue  $\lambda_i$  is the mean square fluctuation along its corresponding principal component. The first principal component accounts for the largest variance, the second for the second largest and so on. Often the first 5% of all principal components suffice to describe 90% of the atomic fluctuations.



# Chapter 3

## Hemoglobin Desorption

In this chapter the shock wave-induced ablation process of water droplets from bulk water will be investigated in atomistic detail by MD simulations. The aim of this investigation is to obtain a detailed mechanical picture of the ablated process as well as of the interaction of the shock wave with the molecule. Especially, the interactions of non-covalently bound complexes with a shock wave, that leads to the ablation of the droplet, are of interest. This investigation finally will give answer to the question, why even non-covalently bound complexes show little fragmentation during the ionization process of the LILBID-MS. Hemoglobin was chosen as complex to investigate the softness of the LILBID method, because hemoglobin is a non-covalently bound tetrameric complex, which is well characterized in experiments [6, 36] and extensively studied in MD simulations.

### 3.1 Methods

To study the ionization process of the LILBID-MS, the human hemoglobin is used. The experimental setup is briefly described in chapter 3.1.1. For a comprehensive description of the experimental setup we refer the reader to the article of Charvat et al. [6].

In the experiments, not only monomers of the hemoglobin, but also dimeric, tetrameric and even quaternary units of the hemoglobin are detected. In addition, it was pointed out that the ablation of water droplets from a water jet is not only a process of evaporation, but is also caused by explosion of the water beam. The characteristics of the explosion like strength and direction can be adjusted, and they influence the distribution of detected fragments significantly. The closer the source of the shock wave (center of irradiation) is placed to the surface of the water jet, the more anisotropic the explosion

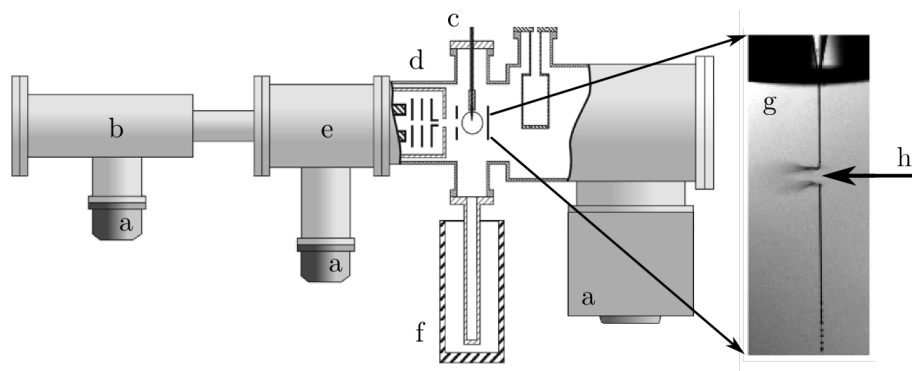


Figure 3.1: Experimental setup for LILBID. **a**: Vacuum pumps. **b**: Time of flight mass spectrometer. **c**: Nozzle for injection of water beam. **d**: Ion optics. **e**: Differential pumping stage. **f**: Cryo trap for water beam. **g**: Zoomed area of water beam. **h**: Infrared Laser beam. [6]

is and the larger the detected complexes of the hemoglobin are.

This leads to the assumption, that a shock wave-induced ablation of water droplets is the reason for the non-destructive characteristic of the ionization process. To test this hypothesis, the influence of a shock wave on hemoglobin is studied by MD simulations in chapter 3.1.2.

### 3.1.1 Experimental Setup

The LILBID-MS setup (Fig. 3.1) consists basically of two parts. A standard Time-Of-Flight (TOF) mass spectrometer and a non-destructive molecule desorption part. The latter consists of a thin water jet with a diameter of  $10 \mu\text{m}$ , which under high pressure (10–20 bar) is ejected into a vacuum chamber. This water jet with a flow speed of  $40 \text{ ms}^{-1}$  contains sodium chloride and hemoglobin. In the vacuum chamber, the conditions within the water jet are close to normal bulk water conditions (room temperature, atmospheric pressure, pH neutral). An infrared laser, whose frequency is tuned to the blue side of the OH bulk absorption band of water ( $2.6\text{--}2.85 \mu\text{m}$ ), is used to irradiate the water beam for 7 ns. Depending on the frequency, it is possible to heat up the water jet throughout or just its surface layer (see Fig. 3.2). If the laser is tuned far to the blue side of the absorption band of bulk water ( $\lambda = 2.65 \mu\text{m}$ ), then the water jet is heated up throughout. In contrast, if the wavelength  $\lambda$  of the laser is close to the absorption band of bulk water  $\lambda = 2.8 \mu\text{m}$ , then just the surface layer of the water jet is heated up. Further, it is possible to shift the center of irradiation on the water jet by shifting the focus of the laser beam.

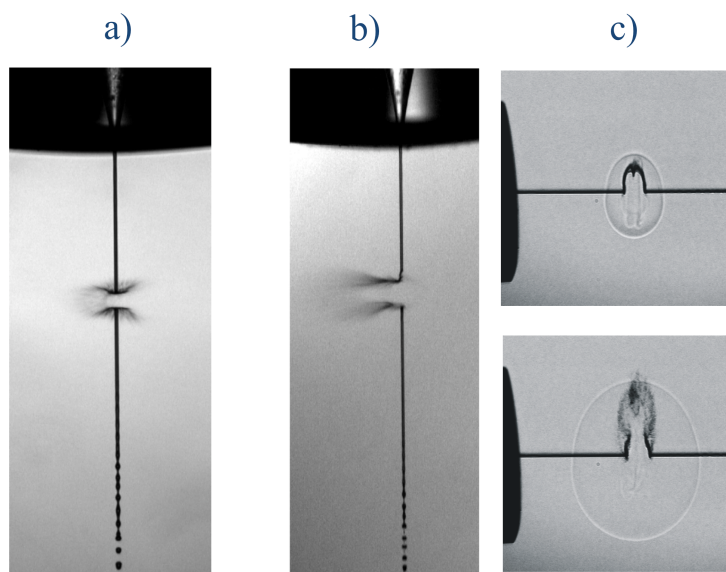


Figure 3.2: The penetration depth depends on the laser frequency. **a)** Greater penetration depth at  $\lambda = 2.65 \mu\text{m}$ . **b)** Smaller penetration depth at  $\lambda = 2.8 \mu\text{m}$ . **c)** Smaller penetration depth results in anisotropic explosion of the water jet [6].

Upon heating of the water jet, a shock wave propagates with a velocity of approximately 2000 m/s [7] through the water jet and leads to ablations of droplets. Perpendicular to the water jet and the laser beam, a small fraction of these droplets enters the ion optics of a TOF mass spectrometer, where the intact tetrameric complex and parts of it are detected (Fig. 3.3). The closer the irradiation center is placed towards the surface of the water jet, the more the distribution of detected complex sizes is shifted to larger complexes. These experiments were done by Ales Charvat, Andreas Bögehold and Bernd Abel. For further details of the LILBID MS method we refer the reader to their publications [6, 7, 1] and the article of Wattenberg [36].

### 3.1.2 MD Setup

To model the shock wave-induced ablation of water droplets from bulk water, a Molecular Dynamics Simulations system was used as drafted in Figure 3.4. At the left side of a water box, which has a vacuum interface on its left and right side, a temperature gradient is applied. This gradient induces a shock wave, which propagates from the left to the right side of the water box. On its way to the other side of the water box the shock wave interacts with the hemoglobin and leads to an ablation of water droplets.

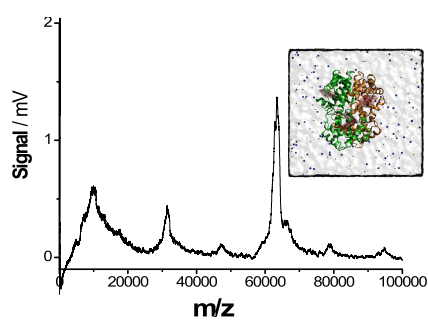


Figure 3.3: Mass spectrum of Hemoglobin. The strongest signal arises from tetrameric complexes [6].

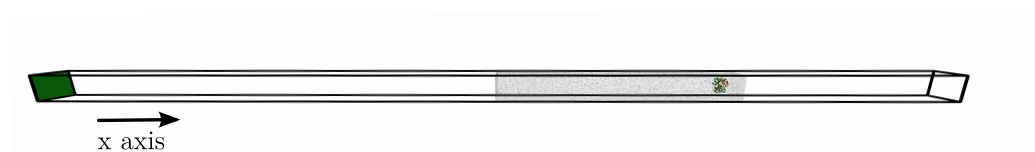


Figure 3.4: MD System Setup. At the left end of the system at  $x=0$  nm an argon wall (green spheres) closes the system. A 80 nm long water box at physiological ion concentration (red and blue dots) is centered in the system, containing a hemoglobin molecule (cartoon representation) at the right end.

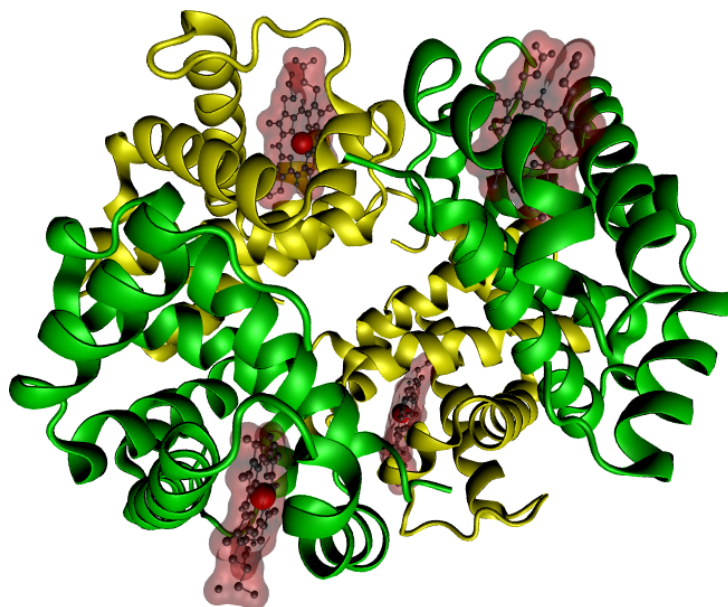


Figure 3.5: Ribbon representation of the deoxyhemoglobin (2DN2) structure.  $\alpha$ -subunits are drawn in yellow (chain A, C),  $\beta$ -subunits in green (chain B, D) and the heme groups in red.

First, the hemoglobin structure used in all MD simulations is introduced, followed by a description of the generation of the shock wave. Finally, the ensemble of performed simulations is described in detail.

### Hemoglobin Structure

Hemoglobin is a globular tetrameric protein, which consists of four globular subunits (Fig. 3.5). Each of the subunits is strongly associated with a heme group. The heme group is a porphyrin, which is covalently bound to an iron ion. The iron ion is the oxygen binding site of the hemoglobin. Oxygen binding is the main function of hemoglobin. Oxygen associated hemoglobin is called oxyhemoglobin, without bound oxygen it is called deoxyhemoglobin. Up to now, more than 440 atomic resolution structures of hemoglobin were solved by x-ray diffraction methods. From this variety of available structures, the deoxyhemoglobin (**2DN2**) obtained by Park et al. in 2006 [32] will be used in this thesis. The crystallized structures are the human hemoglobin unbound (2DN2), associated with oxygen (2DN1) and with carbon monoxide (2DN3). The achieved spatial resolution of 1.25 Å is up to now unmatched.

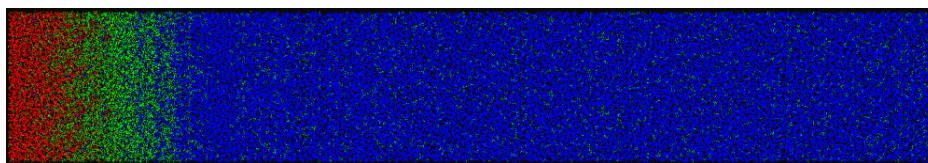


Figure 3.6: Temperature gradient applied to generate a shock wave. Left side temperature 50000 K exponential decaying to 300 K over 12 nm.

### Shock Wave

The shock wave leading to the ablation of water droplets was generated by a temperature gradient as depicted in Figure 3.6. The main characteristics of this shock wave, like penetration depth, temperature gradient and exposure time, were chosen to generate a shock wave, which meets the experimental one in strength and shape.

To meet these specifications, the temperature gradient has an initial temperature  $T_0$  of 50000 Kelvin and decays exponentially, obeying Lambert-Beer's Law (equation 3.1), with  $\alpha = 0.44$  to a final temperature of 300 K,

$$I(d) = I_0 e^{-\alpha d}, \quad (3.1)$$

where  $I(d)$  is the intensity of radiation at a penetration depth of  $d$ .  $I_0$  denotes the initial intensity outside the water box and  $\alpha$  is the absorption coefficient of the water box.

### Ensemble Setup

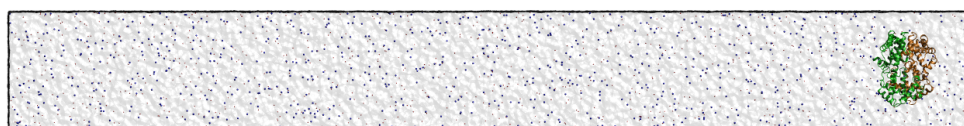
All MD Simulations are based on the structure of Park et al. (2DN2) [32] and were performed using the Gromacs MD simulation package [33] with the GROMOS96 43A1 force field [11]. The hemoglobin was simulated under normal conditions to equilibrate the structure and generate independent conformation for an ensemble of hemoglobin structures. This ensemble was used in combination with large water boxes to simulate the shock wave-induced ablation.

For the equilibration of the hemoglobin structure, the hemoglobin was placed in a rectangular periodic box of about  $11 \times 10 \times 10 \text{ nm}^3$  filled with around 32000 water molecules. The water model used was SPC [20] with internal degrees of freedom constrained by the SETTLE [29] algorithm. To reach physiological salt concentration of 154 mMol/l and to neutralize the system, 87 chloride and 93 sodium ions were inserted in exchange for one water molecule per ion.

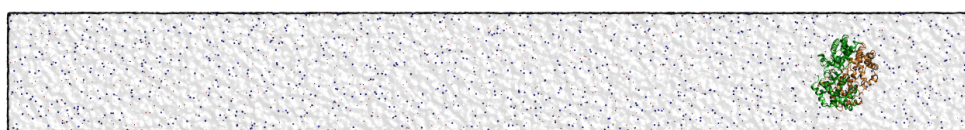
First, the system was energy minimized for 300 steps using the steepest descent method. Then the structure was equilibrated for 80 ns at a temperature of 300 K and a pressure of 1 bar. During the equilibration, the bond length was constrained by LINCS [18], thus allowing a time step of 2 fs. The temperature and pressure were kept constant by coupling to an external bath [3] ( $\tau_T = 0.1$  ps,  $\tau_p = 1$  ps). A twin-range cut-off method was used for the Lennard-Jones interactions. Interactions within 1.0 nm were updated every time step. The Coulomb interactions within 1.0 nm were computed each time step as well. Beyond this cut-off, the Particle Mesh Ewald (PME) [10, 15] method with a grid spacing of 0.12 nm, a switching tolerance of  $10^{-5}$  and cubic polynomial interpolation was used. The hemoglobin structure reached a stable state, based on its backbone RMSD, after 20 ns. The following 60 ns of the equilibration simulation are the source of conformations for an independent ensemble of hemoglobin structures.

Three independent structures from the equilibration were chosen at 78 ns, 79 ns and 80 ns equilibration time to build up the ensemble as shown in Figure 3.7, which was used in all subsequent simulations. These structures with their surrounding water and ions were placed at the right end of a new system box, which is elongated in the x dimension up to 80 nm, with an offset of -5 nm, -10 nm, -15 nm, -20 nm and without offset. The new systems were filled with water and ions similar to the setup of the first equilibration of the hemoglobin. A second equilibration simulation with the same simulation parameters as the former one was performed for 100 ps. The systems sizes were again extended in x dimension up to the final length of 300 nm and the water boxes were shifted by 150 nm in x direction to center them. The systems with an offset in the hemoglobin placement of -15 nm and -20 nm were equilibrated a third time to reduce discontinuities in the potential energy, which have been observed in shock wave simulations, which started after the second equilibration step. To equilibrate the bond and angle terms of the hemoglobin in the third equilibration of 30 ps, no LINCS constraints were used on the hemoglobin. For this last equilibration simulations the same simulation parameters as in the shock wave-induced ablation simulations were used.

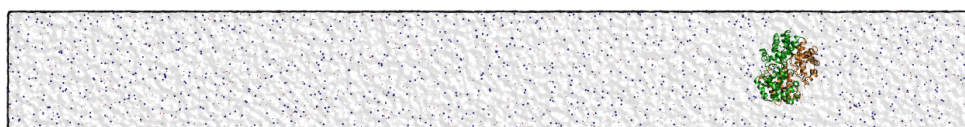
To finally setup the system for the shock wave-induced ablation, a temperature gradient was applied on the water box opposite to the hemoglobin as described in the previous section of this chapter. The initial temperature was 50000 K,  $\alpha=0.44$  and the penetration depth of the temperature gradient from the left side of the water box was 12 nm. The fast molecules from the outer edge of the temperature gradient, which could enter the system from the opposite side via periodic boundary conditions and thus collide with the ablated layer, have be accounted for. To prevent these molecules from jump-



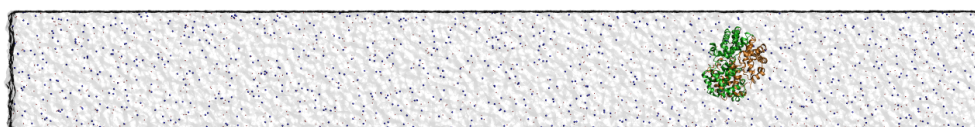
(a) no offset



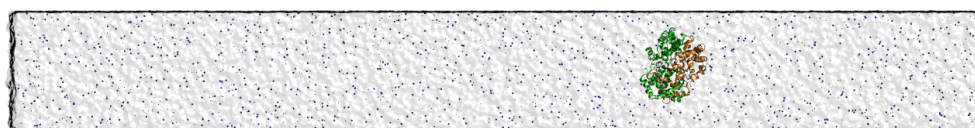
(b) offset -5 nm



(c) offset -10 nm



(d) offset -15 nm



(e) offset -20 nm

Figure 3.7: Hemoglobin placement in the simulation system. The box size is about 80 nm, 10 nm and 10 nm in x-, y- and z-direction, respectively. The ion concentration is 154 mMol/l.



ing across the periodic boundary and reenter the system, a wall of argon atoms was placed 150 nm in front of the water box (at  $x=0$  nm) with its normal vector parallel to the  $x$  axis of the system. The simulations have been performed neither with temperature nor with pressure coupling as micro canonical system. No constrains were used except the SETTLE method for the SPC water model. To ensure energy conservation during the shock wave simulation, a small time step of 0.5 fs had to be used and the neighbour list was updated every time step. Also the Lennard-Jones interactions were adjusted in a way (shift), that the resulting forces from the potential were smoothly reduced to zero between 0.8 nm and 1.0 nm. The electrostatic interaction within 1.2 nm were calculated every time step. Beyond this cutoff, the PME method was used with similar parameters as previous used for the equilibration simulation, only the switching tolerance was lowered to  $10^{-6}$ . Under these conditions, each system was simulated for 150 ps.

## 3.2 Results & Discussion

A typical example of the ablation process is shown in Figure 3.8. From the left hot part of the water box water evaporates to the left side of the system. In the opposite direction a shock wave propagates through the water box and reaches the hemoglobin at around 20 ps, depending on the placement of the hemoglobin. At 150 ps a water layer is ablated in most of the simulations.

### 3.2.1 Shock Wave

The shock wave setup described in section 3.1.2 produced a shock wave with a velocity of roughly 2700 m/s (Fig. 3.9), which is in good agreement with the experimentally observed velocity of around 2000 m/s (chapter 3.1.1). The shock wave velocity was obtained directly from the derivative of its position under the assumption that the velocity was constant until it reached the hemoglobin. The uniformity of the shock wave velocity is shown in Figure 3.9. The density profile of the simulation system visualizes the propagation of the shock wave in a projection along the  $x$  coordinate. The shock front is clearly illustrated by its density maxima in the bulk water phase. The slope in the first 20 ns in all simulations is constant.

The shape of the shock wave, in particular the shock front, i.e. the right shoulder of the density profile of the shock wave in Figure 3.9, is in good agreement with the shape of the shock front models by Chen et al. [9], who has developed a fluid dynamics model for the ablation of water-rich targets by infrared laser pulses at atmospheric pressure. His model is in reasonable

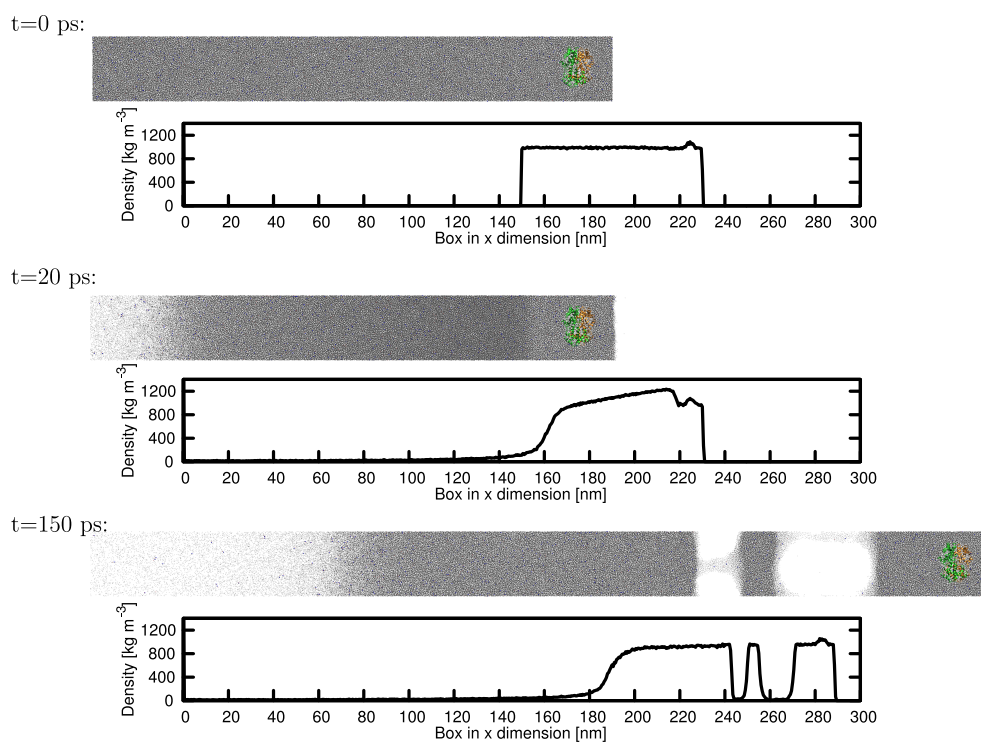


Figure 3.8: Water box containing hemoglobin with corresponding density graphs. t=0 ps: The bulk water phase with hemoglobin before the propagation of the shock wave. t=20 ps: The shock wave 10 nm away from the hemoglobin. t=150 ps: The fully ablated hemoglobin in an ablated water layer.

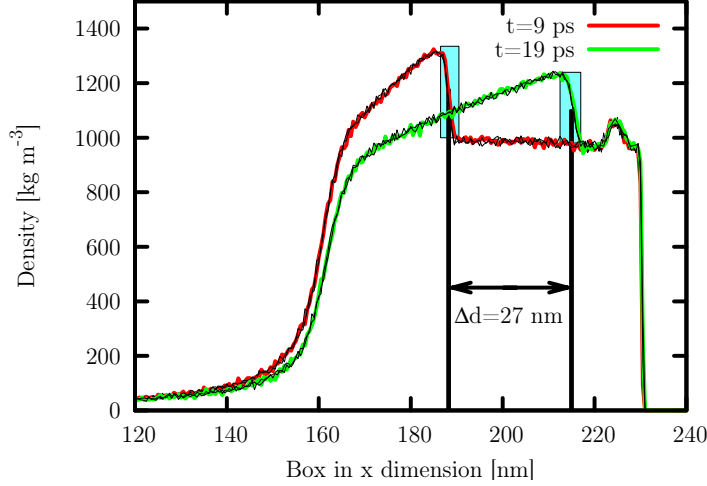


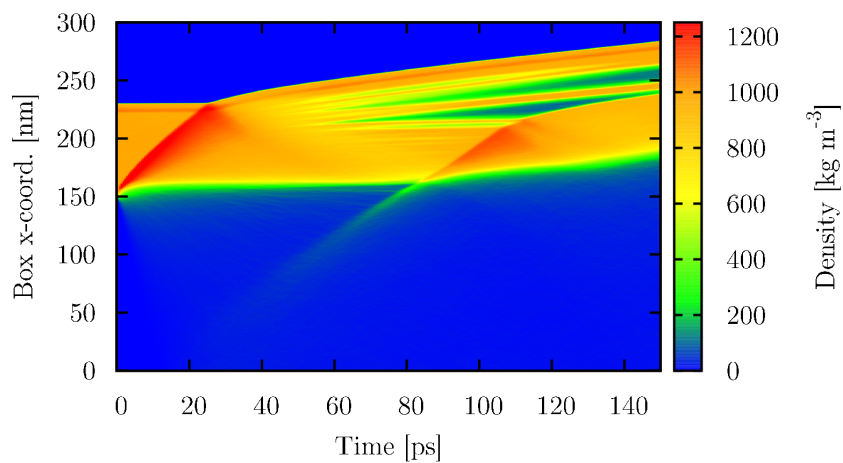
Figure 3.9: Density profile of the MD system along the x axis. The shock wave velocity was obtained from the position difference of the shock wave in its propagation direction at two different time steps. This leads to a shock wave velocity of 2700 m/s. The thin black lines are density plots of the whole ensemble with offset 0 nm.

agreement with data of experimentally obtained shock front displacements.

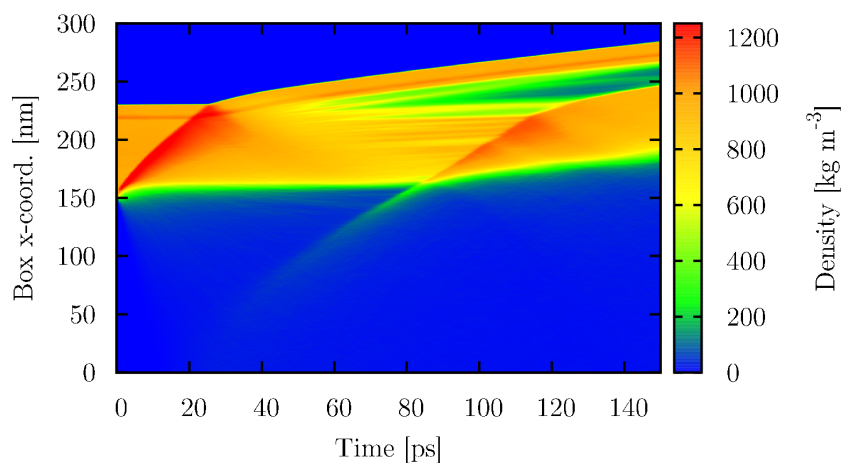
### 3.2.2 Ablation Process

The ablation process for all available placements of the hemoglobin is visualized by the systems density map in Figure 3.9. The density profile is projected onto the x axis, i.e., perpendicular to the shock front. The shock wave on the lower end of the water box and the hemoglobin on the other side are represented by their corresponding density maxima. At the end of most simulations, at least one water layer is ablated. In all hemoglobin placements with an offset smaller than -20 nm, the largest ablated water layer always contains hemoglobin. In all simulations, in which the hemoglobin placement had an offset of -20 nm, the hemoglobin never left the bulk water phase. The shock wave always interacted twice with the hemoglobin. First, during the propagation to the upper bulk water vacuum interface and second after the reflection on this interface.

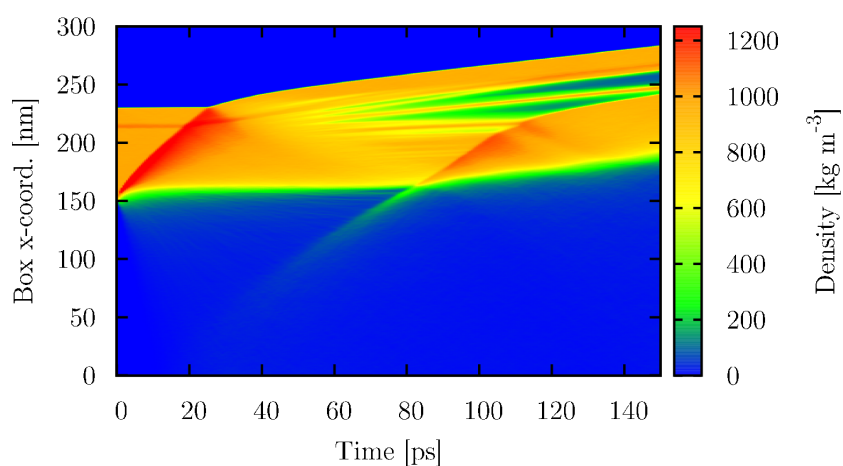
The influence of the initial hemoglobin placement on the ablated layer is illustrated in Figure 3.10. The size and the velocity of the ablated layer are influenced by the initial position of the hemoglobin. A variation in this properties only occurs, when the hemoglobin is placed near the rupture interface



(a) no offset



(b) offset -5 nm



(c) offset -10 nm

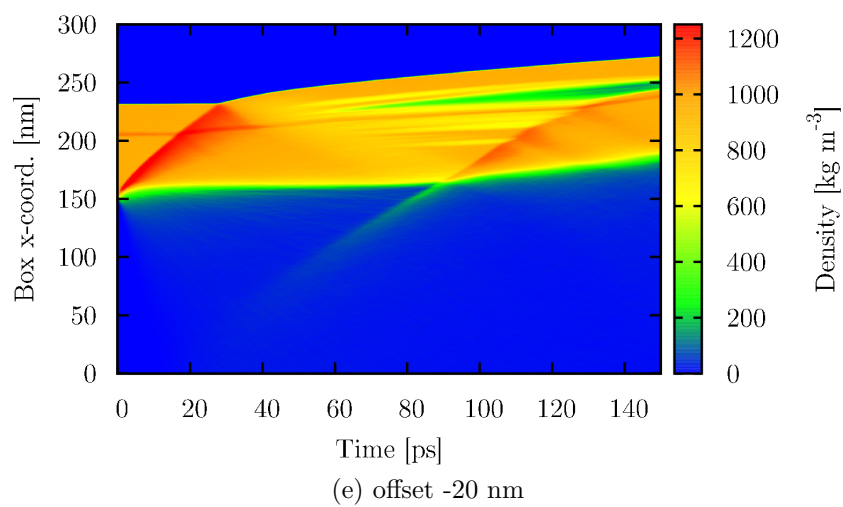
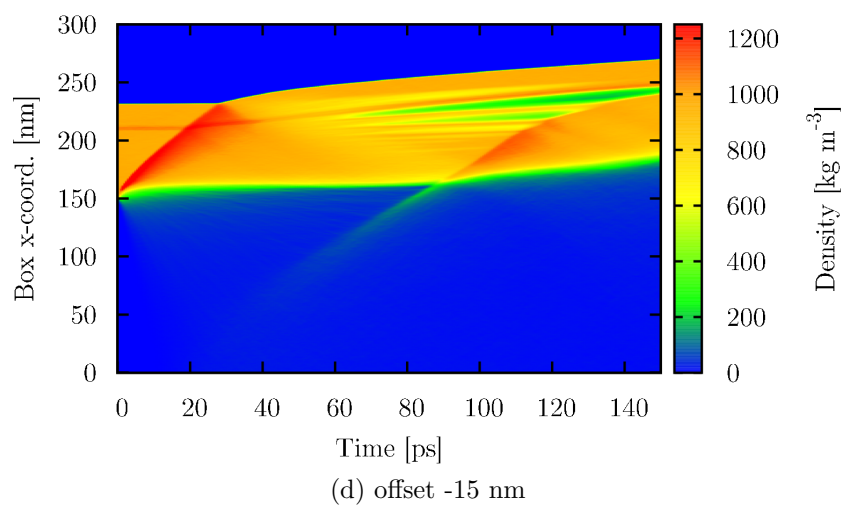
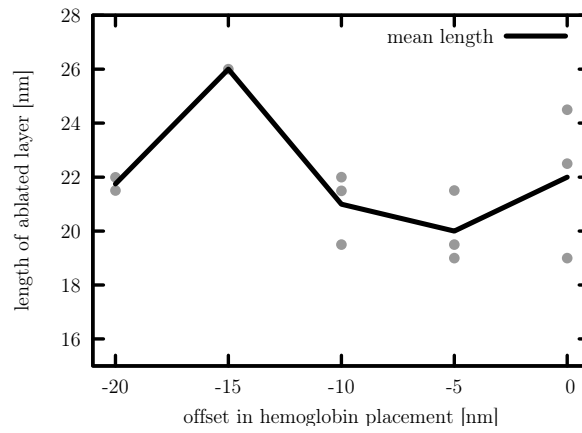
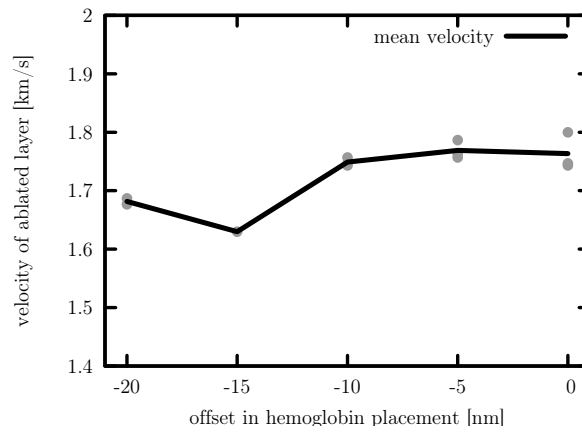


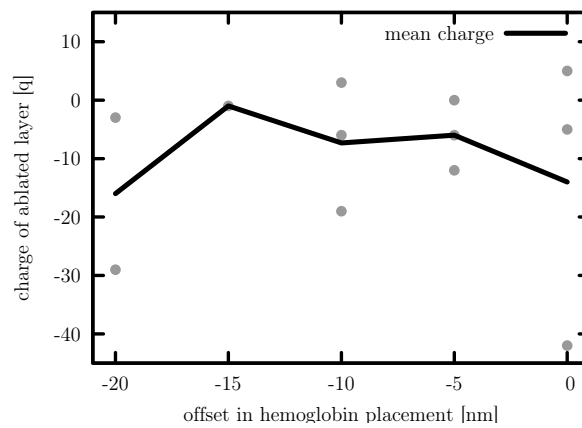
Figure 3.9: Density profile along the x axis, i.e. perpendicular to the shock front, for one representative simulation for each hemoglobin placement. The hemoglobin can be identified as thin upper maxima (red) at upper end of the water box (orange).



(a) Size



(b) Velocity



(c) Charge

Figure 3.10: Ablated layer properties. The size, velocity and charge of the ablated layers of all simulations are shown with respect to the initial placement of the hemoglobin.

of the ablated layer. This is the case in the hemoglobin placement of -15 nm. In this position the hemoglobin interacts with the bulk water phase and the ablated layer. This interaction constrains the ablation process (Fig. 3.9d) and finally yields in a larger and slower ablated layer.

### 3.2.3 Hemoglobin Stability

Figure 3.11 shows the RMSD of the hemoglobin backbone of all simulations. The first peak in the hemoglobin backbone RMSD was simultaneous with the first passage of the shock wave. The second minor peak matched the second passage of the shock wave, after the shock wave was reflected at the water vacuum interface. The peaks of the backbone RMSD describe the deformation of the hemoglobin during the passage of the shock wave. After the initial disturbance of the hemoglobin backbone conformation by the shock wave, the fluctuations decayed within 10 ps in most of the simulations. This leads to the conclusion, that the hemoglobin was only temporally effected by the shock wave and has not taken any major damage, which would result in the fragmentation of the oligomer.

The temperature of the hemoglobin depicted in Figure 3.12 shows a similar result. The slow initial increase of the temperature was most probably due to the release of the LINCS constrains of the hemoglobin. The largest gain in temperature of the hemoglobin was simultaneous with the first passage of the shock wave. The second peak was at the same time as the passage of the reflected shock wave. The water shell around the ablated hemoglobin was heated up to a similar extent as the hemoglobin. Overall the hemoglobin temperature only rises by a small amount. The largest gain in kinetic energy was just due to the compression by the shock wave. After the excitation during the shock wave passage the hemoglobin always cooled down in less than 20 ps.

To describe the conformational change of the hemoglobin during the passage of the shock wave in detail, a PCA on the  $C\alpha$  atoms of the hemoglobin backbone of all simulations has been performed. The PCA was limited to the time of the shock wave passage, i.e. from 12 ps to 38 ps. As shown in Figure 3.13a already 15% of the backbone fluctuations are described by the first eigenvector. The projections of the single trajectories onto the first eigenvector during the passage of the shock wave (Fig. 3.13b) show a similar conformational change in the first eigenvector for all simulations. This conformational change of the hemoglobin backbone structure during the passage of the shock wave is similar to the squeezing of a rubber ball. The conformational change is highly elastic and anisotropic as depicted in Figure 3.14. Thus, the conformational change of the hemoglobin, upon interaction with

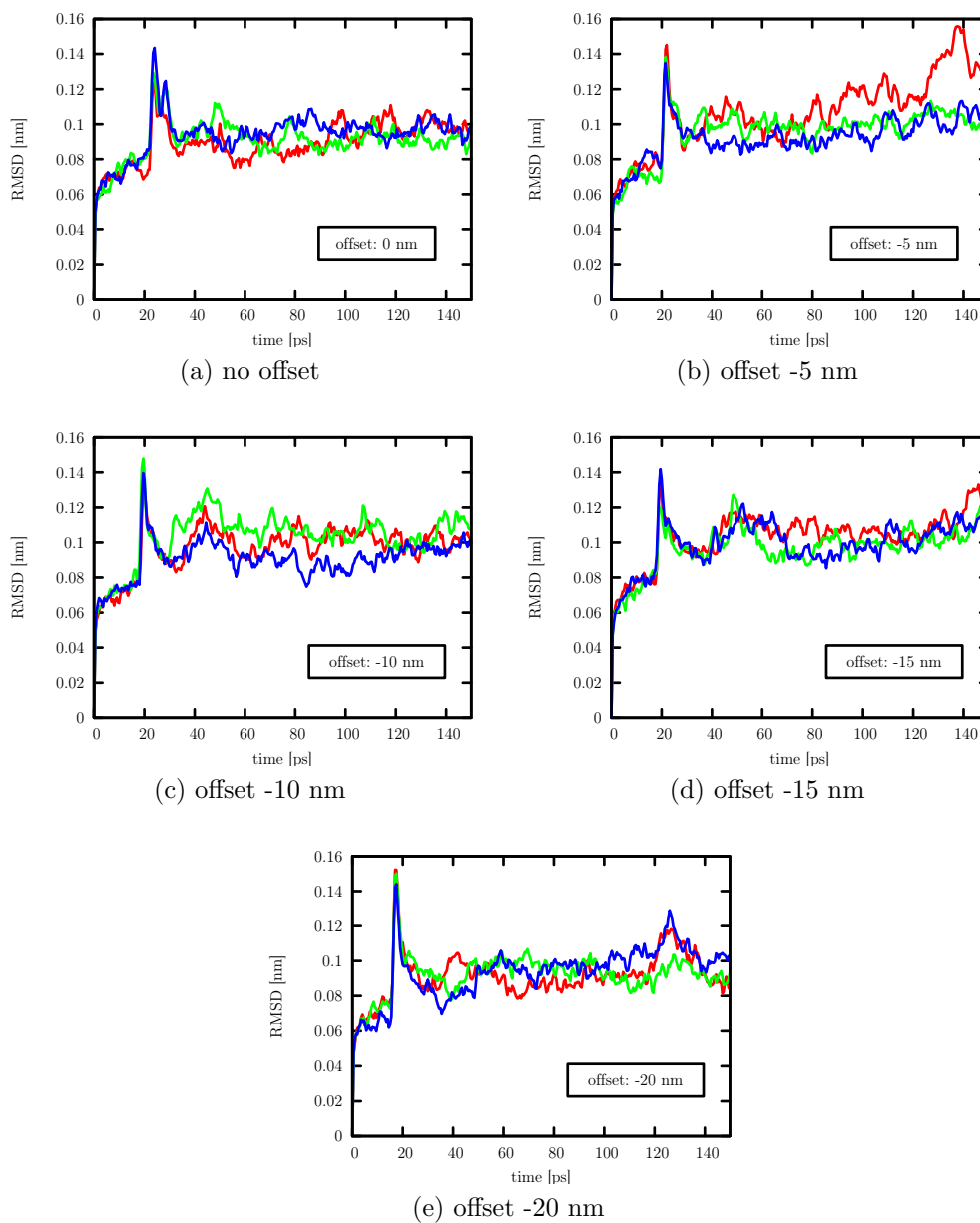


Figure 3.11: Conformational stability. RMSD of the hemoglobin backbone of all simulations with respect to their starting structures.



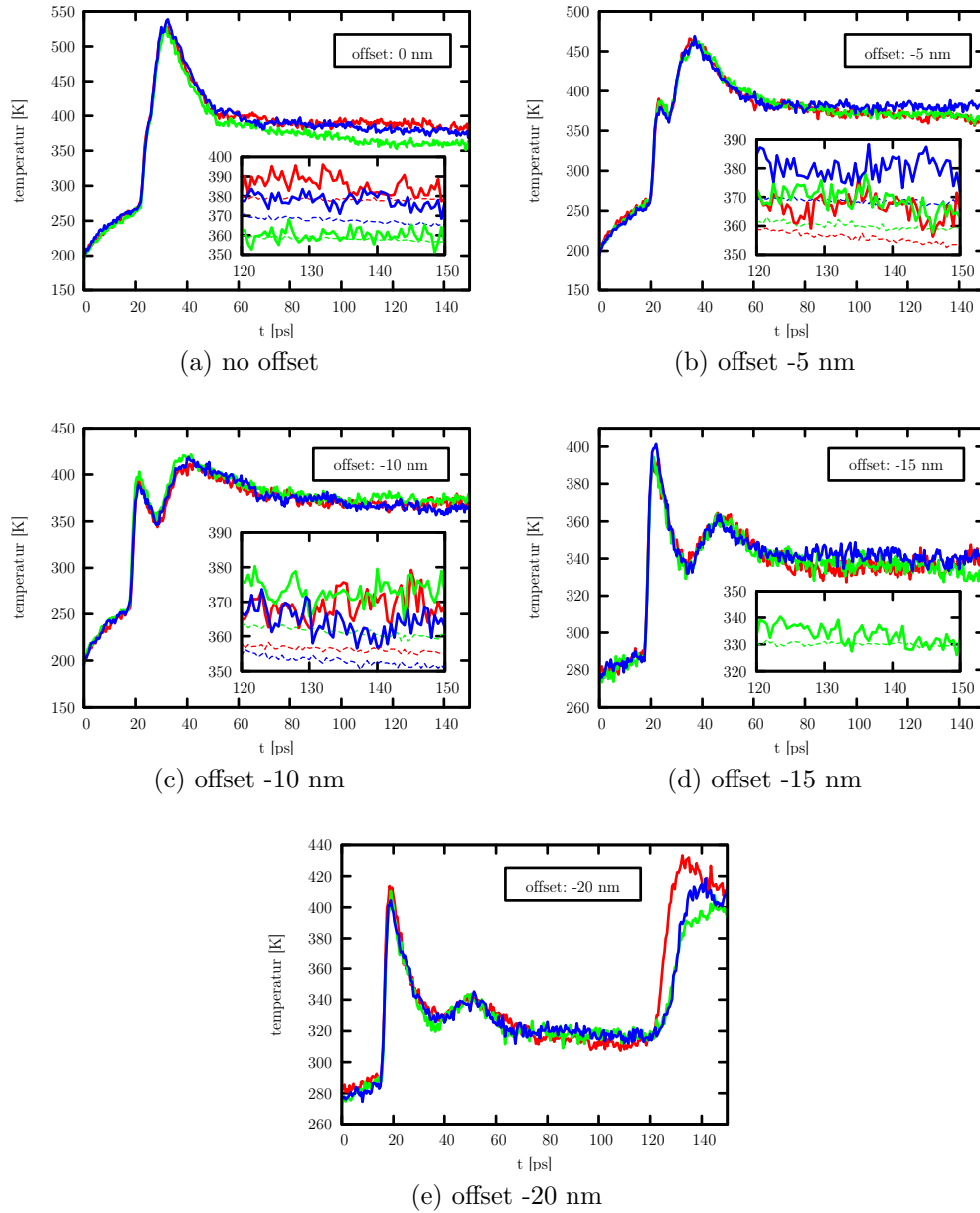


Figure 3.12: Temperature of the hemoglobin. The temperature of the hemoglobin over time for each initial hemoglobin placement from offset 0 nm to offset -20 nm. The insets compare the hemoglobin temperature (solid line) against the temperature of the corresponding water shell (dashed line).

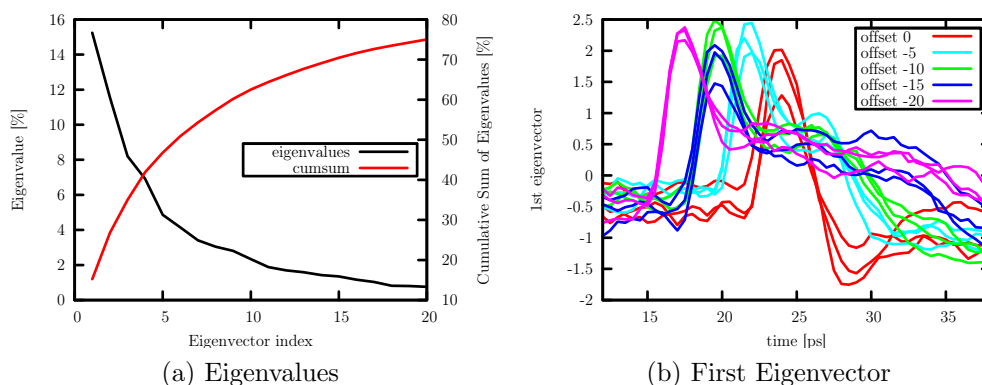


Figure 3.13: PCA of the  $C\alpha$  atoms of the hemoglobin backbone. a) Normalized eigenvalues of the  $C\alpha$  backbone PCA. b) All trajectories projected onto the first eigenvector and sorted by their initial placement of the hemoglobin.

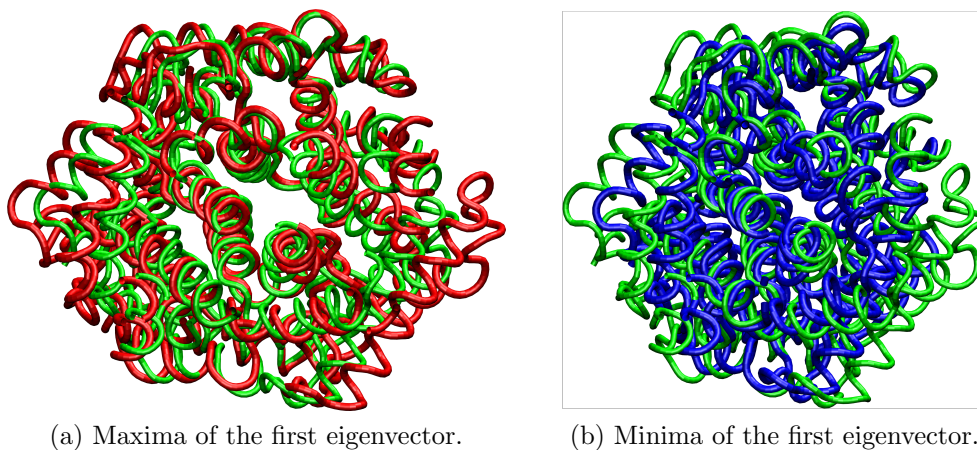


Figure 3.14: Extreme projection of the first eigenvector onto a trajectory. The direction of the shock wave propagation is from left to right. a) Projection of the maxima of the first eigenvector onto a trajectory (red) in comparison to the unperturbed hemoglobin structure (green). b) Projection of the minima of the first eigenvector onto the same trajectory (blue) in comparison to the unperturbed hemoglobin structure (green).

the shock wave, can be described as an adiabatic compression.

### 3.3 Conclusions

The shock wave-induced ablation of hemoglobin was successfully modeled by MD simulations. The strength of the shock wave in MD Simulations was comparable to the one obtained from LILBID experiments [6] and their shape matches the sophisticated model of Chen et al. [9]. Thus, the MD Simulations presented in this work reproduced the experimental shock waves to an extent, which allowed us to investigate the shock wave-induced ablation process at atomistic detail.

The interaction of the shock wave with the hemoglobin was dominated by an adiabatic compression of the hemoglobin during the passage of the shock wave. The hemoglobin stabilized the surrounding water shell during the ablation process, resulting in a many layer water shell. The adiabatic nature of the process did not lead to a large temperature gain neither for the hemoglobin nor for its water shell. Thus, the tetrameric structure of the hemoglobin remained stable during the passage of the shock wave and throughout the rest of the simulations.

One question arose about the size of the water shell. The experimental data showed not more than a few water molecules attached to the hemoglobin, when being detected, in contrast to the larger water shell obtained from MD Simulations. One possibility, how the hemoglobin loses its water shell in the time between ablation detection, is evaporation. But the temperature of the water hemoglobin complex was much too low, that more than one water layer would have been evaporated until the temperature of the water shell converges to around 215 K, as described by Caleman and van der Spoel [4]. When the water hemoglobin complex reaches final temperature, further evaporation is very unlikely. Another pathway how the hemoglobin gets separated from its water shell could be coulomb explosion. In contrast to ESI, the detected charge states of the hemoglobin in LILBID are very low. This is also in good agreement with the MD Simulations. Hence, the charge of the water shell considering its size is far below the Rayleigh limit [5] and thus the occurrence of coulomb explosion of the water shell on its way to the detector is most unlikely.

It was shown that the tetrameric structure of the hemoglobin stays intact during the ablation process and until the simulation ended. It was also shown, that the ablated hemoglobin is always surrounded by a water shell. Further it was shown, that the total temperature gain of the hemoglobin and the water shell is rather small compared to temperature peak both received

during the passage of the shock wave. Thus, MD Simulations revealed the adiabatic nature of the ablation process and give answer to the extraordinary softness of the LILBID ionizations method. But it is still unknown how the analyte gets rid of its water shell.

# Chapter 4

## Charge Mechanism of Droplets

The work of the current chapter of this thesis was done in close collaboration with Dr. Esteban Vöhringer-Martinez. In the previous chapter (Chapter 3) the shock wave-induced ablation process of hemoglobin was investigated in atomistic detail to reveal the nature of the softness of the LILBID ionization method. In this chapter the charge mechanism of the ablated water shell are in the focus of interest. To shed light on the charge process, experiments done with a water jet containing varying ion concentration are investigated with three different models. The models reach from a simple statistical model without any interaction between the ions up to a complexity, which takes not only the ion interaction into account but also the full water dynamics during the ablation process.

First the experiments performed by the Abel group with which we collaborated are introduced. Afterwards, the three models, all describing the charge mechanism, are compared to the experimental data, to reveal the nature of the charge mechanism of the ionization process of the LILBID method.

### 4.1 Experiment

All experiments have been performed by Alexander Beinsen. Thus all experimental data and figures are obtain from him. The experimental setup was similar to the one described in chapter 3.1.1. Instead of hemoglobin at a fixed salt concentration, the experiments were performed without analyte, but with a varying sodium chloride concentration. The salt concentration ranged from  $10^{-6}$  Mol/l to  $10^{-1}$  Mol/l. Further, the sodium ion peaks of the resulting mass spectra (Fig. 4.1) have been summed up to obtain a relationship between salt concentration and measured intensity, i.e. number of charged droplets (Fig. 4.3).

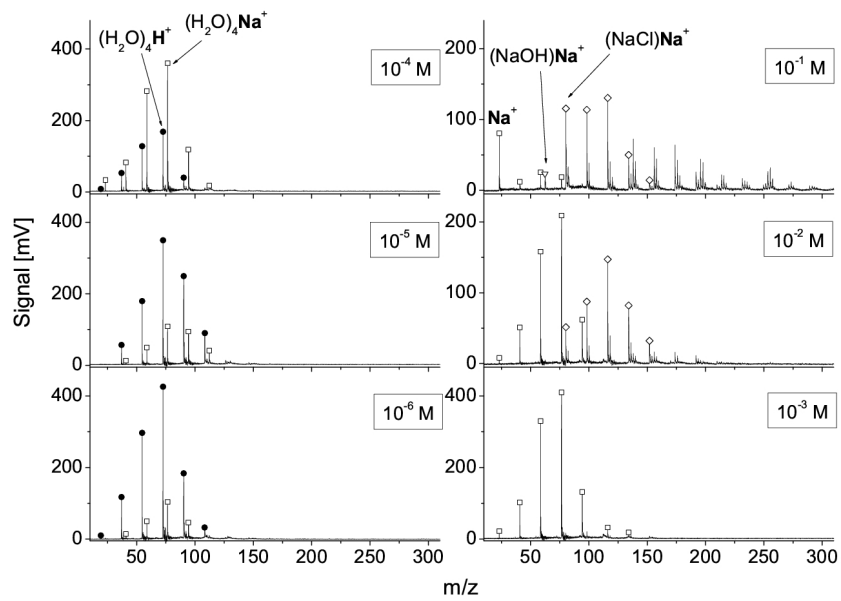


Figure 4.1: LILBID mass spectra. The LILBID mass spectra from sodium chloride solution at six different concentrations, from  $M^{-1}=10^{-1}$  Mol/l up to  $M^{-6}=10^{-6}$  Mol/l. Circles are  $(\text{H}_2\text{O})_n\text{H}^+$  cluster, squares are  $(\text{H}_2\text{O})_n\text{Na}^+$  clusters, diamonds are  $(\text{H}_2\text{O})_n(\text{NaCl})_n\text{Na}^+$  and  $(\text{H}_2\text{O})_n(\text{NaOH})_n\text{Na}^+$  clusters and triangles are  $(\text{NaOH})\text{Na}^+$  clusters.

## 4.2 Methods

The three models used to describe the charge mechanism of the LILBID ionization process are first, a simple statistical model based on the Poisson distribution of non interacting ions, second, a Monte Carlo model of interacting ions and at last, a MD Model, which takes the full dynamics of the ablation process into account at atomistic level.

### 4.2.1 Statistical Model

The basic idea behind the statistical model is to describe the probability distribution of sodium  $P(N_{Na}, k)$  and the probability distribution of chloride  $P(N_{Cl}, k)$  ions in a volume element. The probability distribution of non interacting ions is the Poisson distribution 4.1,

$$P(N_{Na}, k) = P(N_{Cl}, k) = P(N_{Cl, Na}, k) = \frac{N_{Na, Cl}^k}{k!} e^{-N_{Na, Cl}}. \quad (4.1)$$

where  $N_{Na, Cl}$  is the expected number of sodium and chloride ions in the volume element. The number of sodium/chloride ions is  $k$ . The sum of all probabilities, which lead to the same charge difference, is then the charge probability  $P(q)$  (Eq. 4.2) of the volume element,

$$P(q) = \sum_{k_{Na}=k_{Cl}=0} \sum \frac{N_{Cl, Na}^{k_{Na}+k_{Cl}}}{k_{Na}! k_{Cl}!} e^{-2N_{Cl, Na}} \delta(k_{Na} - k_{Cl} - q). \quad (4.2)$$

where  $q$  is the charge of the volume element.

If an uncharged system of non interacting ions is divided into subsystems, these subsystems are charged (Fig. 4.2) according to Equation 4.2.

### 4.2.2 Interacting Model

To account for the Coulomb interaction of the ions, Monte Carlo simulations as described in chapter 2.2 have been performed for all ion concentrations used in the experiment and additionally for 15 mMol/l and 154 mMol/l, to also investigated the physiological salt concentration. The MC system box was cubic with an edge length of 18 nm and contained only sodium and chloride ions. The water interaction was implicitly accounted by the relative static permittivity  $\epsilon_r$  of 80.35. The size of the ions was included with by an minimum mutual distance of 0.4 nm as described by Metropolis et al. [28]. The temperature was 290 K. The boundaries have been extended by

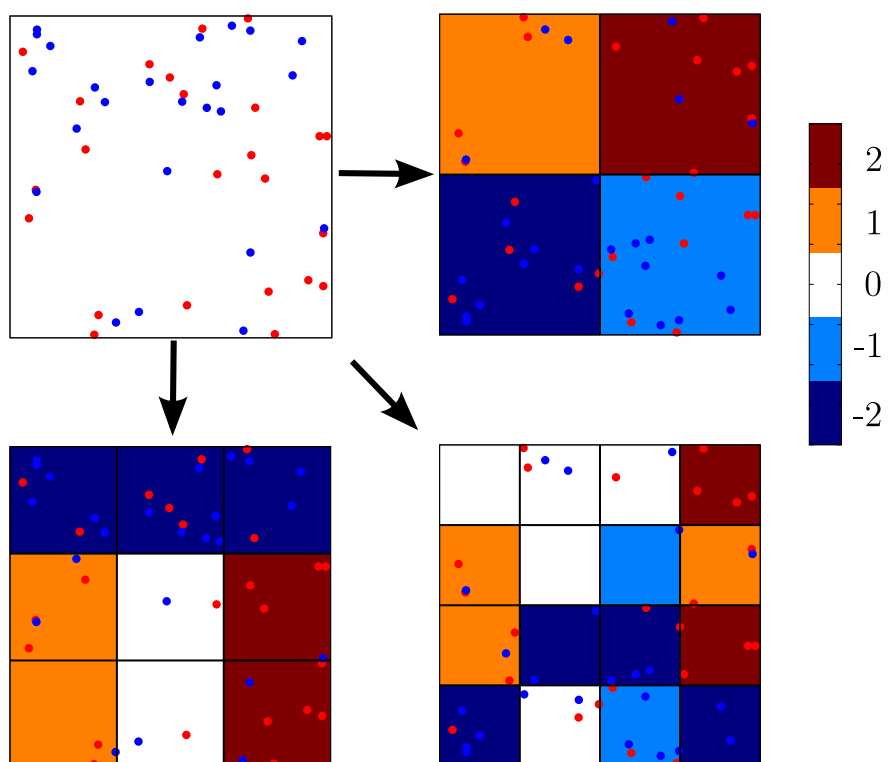


Figure 4.2: Charge mechanism of statistical model. Subsystems of a neutral system are charged, depending of there partition. Sodium is red and chloride is blue. The charge of a system is marked by their background color.



the threefold Debye length to avoid disturbance of the ion distribution in the system box.

Each MC simulation was equilibrated until the total energy of the system was converged to  $\Delta E/E = 10^{-7}$ . For faster convergence the placement distance of the ions was coupled to the ratio of accepted to rejected configurations. The placement distance was increased by ten percent, when the ratio of accepted to rejected configurations was above 0.5, decreased by the ten percent, when the ratio of accepted to rejected configurations was below 0.5 and otherwise kept constant. After energy convergence has been reached,  $10^6$  Monte Carlo steps has been performed to sample the ion distribution. For each ion concentration the charge distribution was derived by counting the ions in the center cubic volume of  $5831 \text{ nm}^3$  and subtracting the number of sodium ions from the number of chloride ions. To achieve a converged charge distribution, the counting of the ions in the central box has been performed for 125 boxes for each salt concentration.

### 4.2.3 Dynamical Model

To describe the full dynamics of the charge process during the ablation of water layers, MD simulations have been performed. The system setup was similar to the MD setup described in chapter 3.1.2, except for the size of the water box, which has been  $50 \times 4 \times 4 \text{ nm}^3$ . Two different ion concentrations were used. One of 15 mMol/l, which was obtained by adding 8 sodium and 8 chloride ions and 154 mMol/l, which was achieved by adding each 75 sodium and 75 chloride ions into the water box in exchange for one water molecule each. The ions were placed according to the Debye Hückel Potential and their placement was then refined by a Monte Carlo simulation. The MC routine used periodic boundary conditions and was performed for  $8 \times 10^6$  steps.

The parameters to model the shock wave were the same as described in chapter 3.1.2. The MD parameters to compute the ablation process were the same as used in the computation of the hemoglobin ablation described in chapter 3.1.2. Under these condition 414 trajectories were obtained at an ion concentration of 15 mMol/l and 597 trajectories at an ion concentration of 154 mMol/l.

## 4.3 Results & Discussion

The charge distribution of the statistical model was linearly fitted to the experimental data as depicted in Figure 4.3. The fit of the statistical model to the experimental data is only matching for low ion concentrations. This

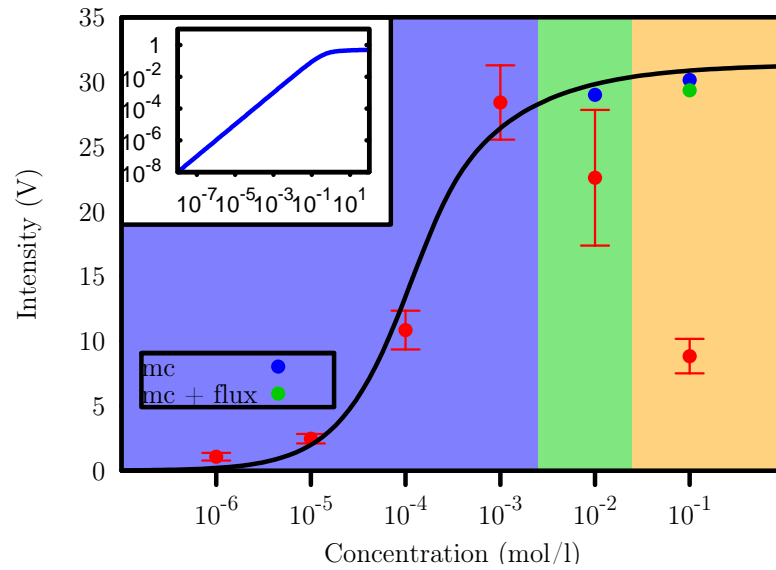


Figure 4.3: Fit to experimental data. The statistical model (black line) was fitted to the experimental data (red). For higher concentrations the experimental data was compared to Monte Carlo simulations (blue) and for 0.1 Mol/l the Monte Carlo simulations have been modified by the full dynamical model (green). The inset shows the statistical model fit to the experimental data in double logarithmic presentation. The background color shows, which model is necessary to describe the charge distribution; blue statistical model, green MC, yellow MD.

result is in good agreement with findings of Dodd [12] in oil droplets, especially the linearity which is shown in the inset of Figure 4.3. From the fit of the statistical model to the experimental data, it is possible to obtain an estimate of the droplet volume  $V$  of around  $5600 \pm 3200 \text{ nm}^3$ , via the relation  $V = N/N_A \cdot 10$ , where  $N$  is the number of expected ions in the volume  $V$  and  $N_A = 6.022 \cdot 10^{23} \text{ mol}^{-1}$  is the Avogadro constant.

The droplet volume was used in the Monte Carlo simulations to refine the prediction of the experimental data at higher ion concentrations. Figure 4.4 shows that for ion concentrations lower than 15 mMol/l the statistical model matches the findings of the MC simulations. Thus, the correction of the statistical model for ion concentrations higher than 1 mMol/l were necessary. The correction of the charge distribution, taking the Coulomb interaction between ions into account, is shown in Figure 4.3.

To include the dynamics of the ablation process in the modeled charge distribution, MD simulations were used. To analyze the trajectories a program called ablation analyzer was written, which recognizes the ablated layers from their formation until their total ablation. The program also keeps track of possible water bridges, as depicted in Figure 4.5 and the trajectories of ions in the water bridges. The dynamics of the water bridges and their containing ions are the main properties describing the ion flux during the ablation process. The ion flux and the charge distribution before and after the ablation are depicted in Figure 4.6. The charge distributions before the ablation took place, are similar to the charge distribution obtained from MC simulations, because the initial placement of the ions in the MD simulations was refined by MC simulations, which take the Coulomb interaction into account. The narrowing of the charge distribution of the ablated layer in comparison to the charge distribution before the ablation is a result of the dynamics, i.e. the ion flux, during the ablation process. The ion flux is the flux of ions through the water bridges during the ablation process. The influence of the ion flux in the water bridges is only significant for ion concentration higher than 15 mMol/l.

Now the question arises, if this ion flux is sufficient to describe the narrowing of the charge distribution during ablation. Therefore, the flux obtained from the 597 trajectories with an ion concentration of 154 mMol/l was used to build up a substitution matrix, which describes how the ion flux in the water bridges changed the charge distribution during the ablation process. Now, the charge distribution after the ablation is compared to the charge distribution before the ablation, which is corrected by the ion flux with the substitution matrix shown in Figure 4.7. The two compared distribution are matching and thus the ion flux is the main mechanism, which narrows the charge distribution during the ablation process.

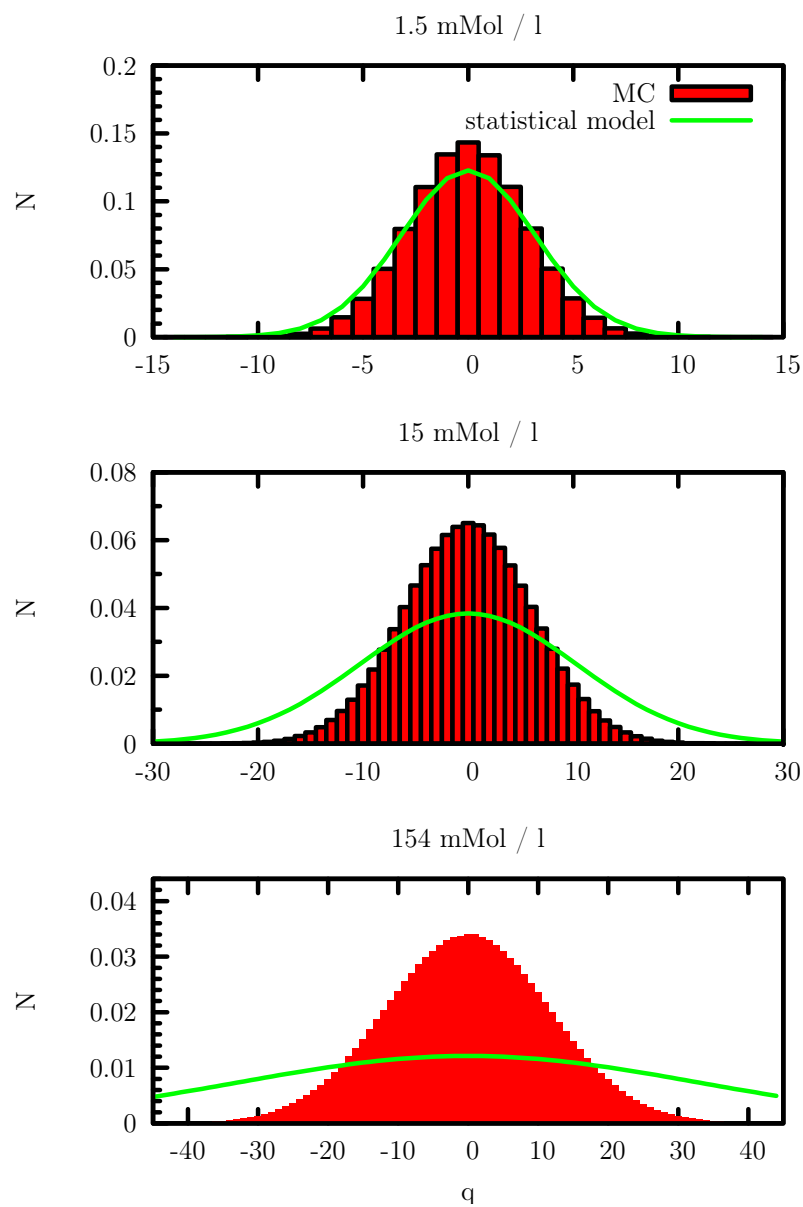


Figure 4.4: Comparison of MC simulations to statistical model. The charge distributions were obtained for a volume of around  $5830 \text{ nm}^3$ .

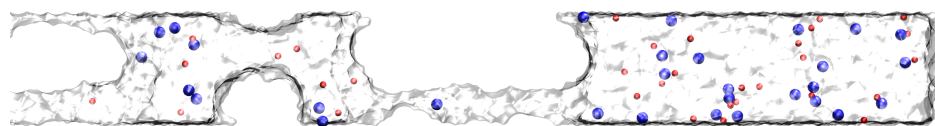


Figure 4.5: Ablation process. The ablation process at an ion concentration of 154 mMol/l at time 32.5 ps. The water surface is represented as a transparent area, sodium as red spheres and chloride as blue spheres.

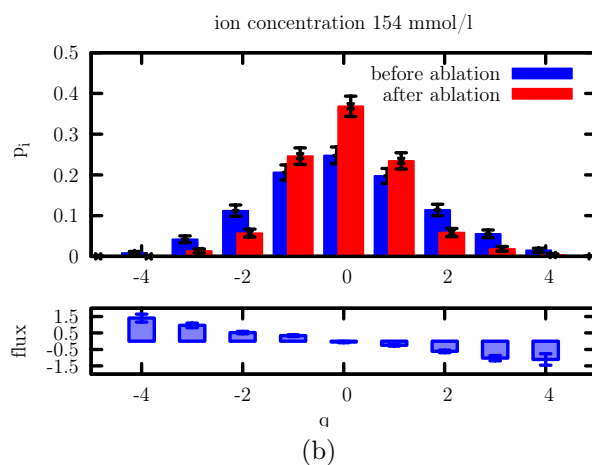
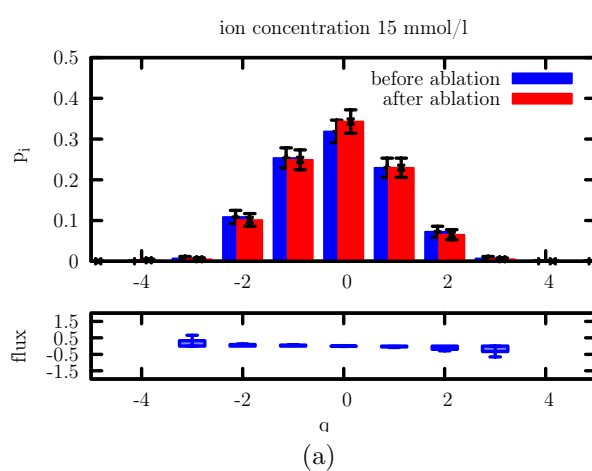


Figure 4.6: Influence of ion flux on charge distributions. The charge distribution before the ablation (blue) are compared to the charge distribution of the ablated water layers (red). The error bars denote statistical errors. The smaller graph shows the ion flux during the ablation process.

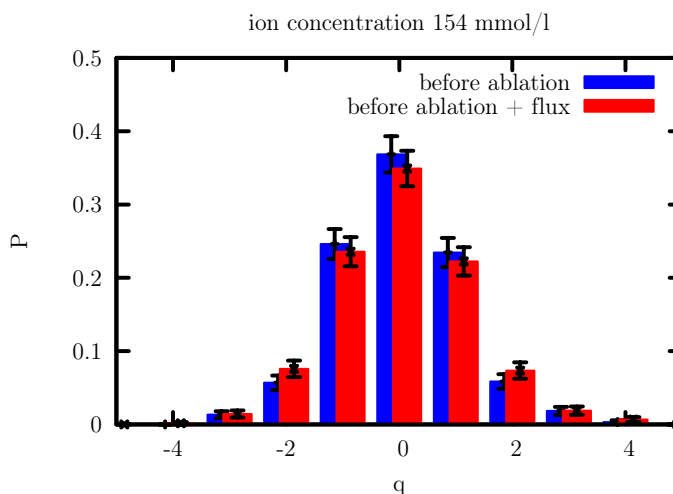


Figure 4.7: Validation of the flux model. The ion flux added to the charge distribution before the ablation (red) is compared to the charge distribution of the ablated layer (blue). The error bars denote statistical errors.

To describe the influence of the ion flux on larger system as used in previous MC simulations, the substitution matrix was extended. Therefore, a normal distribution was fitted to each row of the substitution matrix. The means of these Gaussian distribution were linearly fitted as shown in Figure 4.8. The extended substitution matrix was then used to correct the charge distributions of larger systems used in MC simulations. To compare the influences of the Coulomb interaction and the ion flux on the charge distribution obtained from the statistical model, Figure 4.9 shows the charge distribution of all three models at an ion concentration of 154 mMol/l. At this ion concentration additional effects, each model takes into account, doubles the probability of uncharged water boxes. Finally, the charge distribution of MC simulations, corrected by the ion flux, have been compared to the experimental result (Fig. 4.3). Neither the correction obtained from the MC simulations nor the corrections done by accounting the ion flux were able to explain the experimental result for ion concentrations higher than  $10^{-3}$  Mol/l.

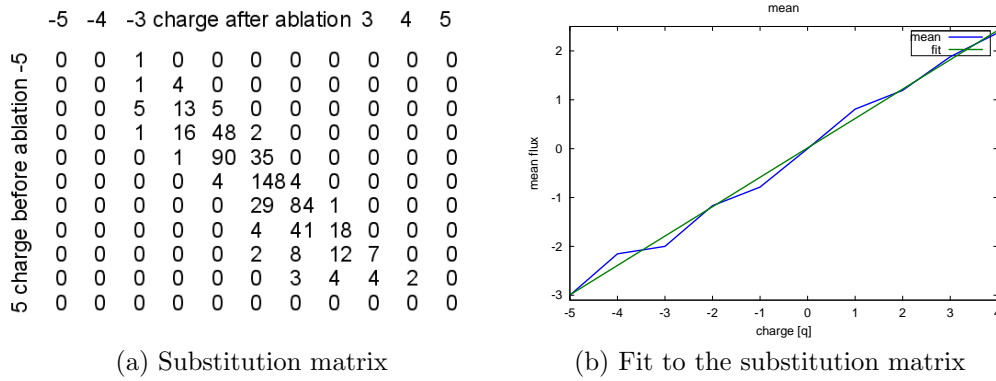


Figure 4.8: Linear fit to the substitution matrix. a) The substitution matrix derived from the ion flux, which was obtained from the trajectories at an ion concentration of 154 mMol/l. b) Each row of the substitution matrix was fitted to a normal distribution. The means of these Gaussian distributions (blue) were linearly fitted (green).

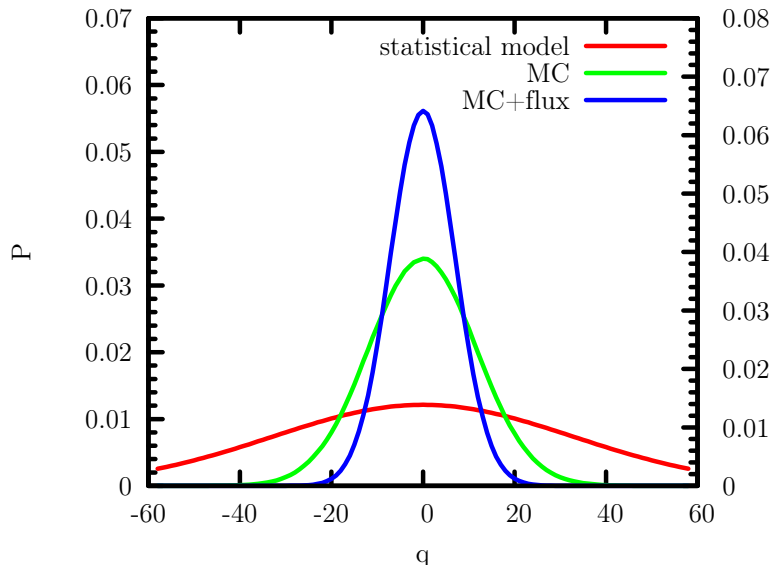


Figure 4.9: Comparison of all three models. All three models describe the charge distribution of a water box with an ion concentration of 154 mMol/l and a volume of around 5830 nm<sup>3</sup>.

## 4.4 Conclusion

The charge mechanism of water droplets was sufficiently described by the statistical model up to an ion concentration of  $10^{-3}$  Mol/l (Fig. 4.3). This conclusion agrees with the findings of Dodd [12] about charge distributions in oil droplets. The ability to analytically describe the charge mechanism of water droplets up to a certain ion concentration, enables us to estimate the volume of the ablated droplets.

The estimation of the volume of the ablated water droplets makes it possible to describe the charge mechanism with a more sophisticated model, which accounts also the Coulomb interaction between the ions by MC simulations. The results of the MC simulation are similar to those obtained from the statistical model up to an ion concentration of  $10^{-3}$  Mol/l and then exceed those of the statistical model at higher ion concentrations. The charge distributions obtained from MC simulations in comparison to those from the statistical model become narrower, i.e. the probability of uncharged droplets rises (Fig. 4.9). This would lead to a lower intensity as predicted by the statistical model. This trend is also shown by the experimental findings (Fig. 4.3), although the absolute numbers are not matching.

To verify that the MC approach describes the charge distribution sufficiently, MD simulations for the two highest ion concentrations have been performed. It was shown, that the dynamical aspects, which the MD simulations added to the description of the charge mechanism, are only relevant for the highest investigated ion concentration (Fig. 4.6). MD simulations revealed, that at this ion concentration the ion flux occurring in water bridges during the ablation process (Fig. 4.5) has a strong influence onto the charge distribution. The ion flux neutralizes the ablated layer during the ablation process, leading to less charged layers. This result is also in agreement with the experimental trend to have less intense signals at higher ion concentrations, i.e. lower number of charged droplets.

Although neither the static MC approach nor the MD approach are able to describe the experimental data quantitatively, both are able to describe the charge mechanism qualitatively. One problem of the low quantitative agreement between model and experiment may be the experimental difficulty to take all sodium associated events into account at high ion concentrations. The higher the ion concentrations are, the broader the corresponding charge distributions are (Fig. 4.4). This leads to highly charged states at high ion concentrations. But in the LILBID-MS spectra at high ion concentrations, the higher charged states ( $q_i/3$ ), are hidden in a continuum at low  $m/z$  values. It is not possible to identify the higher charged states in the continuum at low  $m/z$  values and thus they are not taken into account, when obtaining



the total measured intensity. Thus, taking only the low charged states into account for obtaining the intensity experimentally, would explain why the models are able to describe the experimental findings at low ion concentrations, when only low charged states are forming the charge distribution, but fail to describe the experimental intensities quantitatively for higher ion concentrations, when the higher charged states are the majority of the charge distribution. Unfolding of the complete charge distribution obtained from the models around experimentally identified peaks in the measured spectra, may reconstruct the continuum at low  $z/m$  values and thus reveal the hidden high charge states in the spectra. By taking this revealed high charge states into account, the intensity derived from the spectra at high ion concentration would increase.

This work revealed different aspects of the charge mechanism of the LILBID ionization method. In some points the developed models directly describe the experimental findings and in others they suggest possibilities to refine the analysis of the measured spectra.



# Chapter 5

## Summary & Conclusion

The goal of this work was to investigate the ionization mechanism of the LILBID-MS method and to answer the three main questions, which arise regarding this process. First, why does the ablation process, the most likely pathway of non destructive ionization, leave even non-covalently bound complexes, like hemoglobin, intact, despite the high temperatures and pressures occurring during the passage of a shock wave? Second, how does the analyte, in this case the hemoglobin, lose its water shell in the time between ablation and detection? And last, what mechanisms are leading to the charge of the ablated droplets?

The first question was addressed in chapter 3 by MD methods to simulate the ablation process of hemoglobin. First, it was validated, that the shock wave-induced ablation process simulated by MD reproduces the experimental conditions. Then, the influence of the shock wave on the hemoglobin and its surrounding water shell was investigated.

During the passage of the shock wave, the hemoglobin was elastically and anisotropically compressed. This interaction of the shock wave with the hemoglobin neither lead to the fragmentation of the analyte nor to a large gain in its kinetic energy. Unexpectedly, the temperature gain of the hemoglobin and its surrounding water shell after the passage of the shock wave was below 60 K. Only during the passage of the shock wave, one high peak in the temperature profile of the hemoglobin occurred per transition. This peak was only due to the elastic compression of the hemoglobin.

The interaction of the hemoglobin with the shock wave can be summarized as adiabatic compression of the hemoglobin and thus does not result in its fragmentation.

This leads directly to the second question, which was also addressed in

chapter 3. It was shown, that the water shell around the ablated hemoglobin consists of many water layers and its gain in temperature was below 60 K. This is in agreement with results, based on a statistical description of the charge process of water droplets (chapter 4), which show that the volume of the ablated water droplet is around  $5000 \text{ nm}^3$ . Finally, it was shown that the charge of the ablated layers is below the Rayleigh limit. This is also consistent with findings in chapter 4 based on three different models, describing the charge distribution of the ablated water shell.

But how does the hemoglobin loose its water shell? One possibility is evaporation. But on a  $\mu\text{s}$  timescale, which is the time between ablation and detection in the experiment, a temperature increase below 60 K would only lead to the evaporation of the outermost water layer, as shown by Coleman et al. [4]. This renders the hypothesis, that evaporation is the process leading to the loss of the water shell, very unlikely.

Another possible explanation would be Coulomb explosion as in the ionization process of ESI. However, in contrast to ESI, the charge states of the analyte in LILBID are very low. The charge of the ablated layer is far below the Rayleigh limit and thus, Coulomb explosion is not likely. Therefore, the mechanism dominating the loss of the water shell around the analyte is still unknown, but evaporation and Coulomb explosion can be ruled out in all likelihood.

The last main question concerning the mechanism governing the formation of charged ablated droplets was addressed in chapter 4. We were able to identify three regimes in the experimental measure dependency of the signal intensity to the salt concentration.

The first regime is below a salt concentration of  $10^{-2} \text{ Mol/l}$ . There, the charge distribution of ablated water droplet is well described by a statistical model, which is only based on the Poisson distribution of the ions. The second regime is around a salt concentration of  $10^{-2} \text{ Mol/l}$ . There, the influence of the Coulomb interaction between the ions has to be taken into account to describe the charge distribution of the ablated layers. We revealed that only the spacial partition of the ions prior to the ablation is of importance. The dynamics during the ablation process did not show a significant influence on the charge distribution at this salt concentration. The third and last regime, we were able to reveal, is around a salt concentration of  $10^{-1} \text{ Mol/l}$ . In this regime, the full dynamics of the ablation process, i.e. the ion flux, has to be accounted to describe the charge distribution of the ablated water layers sufficiently. This ion flux, is the flux of ions through water bridges, which are formed during the ablation process between the ablated layers themselves and to bulk water. Surprisingly, this ion flux is the major process describing

the difference between the charge distributions in regime two and three.

We are able to describe the charge distribution of the ablated water droplets up to a salt concentration of  $10^{-3}$  Mol/l quantitatively and qualitatively, with a simple statistical model. This model allows us to obtain the size of the ablated water droplets from the experimentally measure dependency of the signal intensity to the salt concentration. Further, we are able to describe the charge distribution for the salt concentrations of  $10^{-2}$  Mol/l and  $10^{-1}$  Mol/l qualitatively with respect to the experiment, although our findings did not match the experimental observations quantitatively. This may be due to the difficulties to analyze the experimental spectra at these high ion concentrations.

These spectra have a high continuum content at low  $m/z$  values, which makes it impossible to identify single peaks in this continuum region. Thus, higher charged droplets are hidden in this continuum region and are not accounted in the experimentally derived intensities. But our developed models allow us to the describe the charge distributions at higher salt concentrations. This may help to refine the analysis of the experimental data and to reveal this hidden events as proposed in chapter 4, by modeling the continuum content in the LILBID-MS spectra with the help of the calculated charge distributions at high ion concentrations.



# Chapter 6

## Appendix

### Abbreviations

Molecular Dynamics (MD)

Laser-Induced-Liquid-Beam-Ion-Desorption (LILBID)

Mass Spectrometry (MS)

Time-Of-Flight (TOF)

Electrospray Ionization (ESI)

Matrix-Assisted Laser Desorption/Ionization (MALDI)

Monte Carlo (MC)

Potential Energy Surface (PES)

Principle Component Analysis (PCA)

## Curriculum Vitae

Frank Wiederschein  
Bühlstrasse 9  
37073 Göttingen  
Geb. am 18.11.1978 in Peine

Ledig, deutsch

### Studium

04/2001–04/2005:

Physikdiplom an der Universität Stuttgart;

Diplomarbeit: Untersuchung des Aggregationsverhaltens des TNF-Rezeptors mittels Molekulardynamiksimulationen (Wrachtrup, Seifert)

Wahlfächer: Biophysik (Wrachtrup), Kern- und Elementarteilchenphysik (Kneissl)

06/2004–06/2004:

Highlights der Physik Stuttgart;

3D-Proteinkino

10/2002–10/2003:

Wissenschaftliche Hilfskraft am 2. Physikalischen Institut der Universität Stuttgart;

Mitarbeit am Grenoble GigaNMR Projekt: Entwicklung von Probenköpfen (Mehring, S. Krämer)

10/1998–04/2001:

Physikvordiplom an der Universität Stuttgart

### Schulbildung

11/1991–07/1998:

Abitur am Christian Gymnasium Hermannsburg;

Leistungskurse: Mathematik und Physik

Prüfungsfächer: Latein und Religion



# Bibliography

- [1] B. Abel, A. Charvat, U. Diederichsen, M. Faubel, B. Girmann, J. Niemeyer, and A. Zeeck. Applications, features, and mechanistic aspects of liquid water beam desorption mass spectrometry. *International Journal of Mass Spectrometry*, 243(2):177–188, May 2005.
- [2] A. Amadei, A. B. Linssen, and H. J. Berendsen. Essential dynamics of proteins. *Proteins*, 17(4):412–425, Dec 1993.
- [3] HJC BERENDSEN, JPM POSTMA, WF VANGUNSTEREN, A DINOLA, and JR HAAK. MOLECULAR-DYNAMICS WITH COUPLING TO AN EXTERNAL BATH. *JOURNAL OF CHEMICAL PHYSICS*, 81(8):3684–3690, 1984.
- [4] Carl Caleman and David van der Spoel. Temperature and structural changes of water clusters in vacuum due to evaporation. *J Chem Phys*, 125(15):154508, Oct 2006.
- [5] Carl Caleman and David van der Spoel. Evaporation from water clusters containing singly charged ions. *Phys Chem Chem Phys*, 9(37):5105–5111, Oct 2007.
- [6] A. Charvat, A. Bgehold, and B. Abel. Time-resolved micro liquid desorption mass spectrometry: Mechanism, features, and kinetic applications\*. *Aust. J. Chem.*, 59(2):81–103, March 2006.
- [7] A. Charvat, B. Stasicki, and B. Abel. Product screening of fast reactions in ir-laser-heated liquid water filaments in a vacuum by mass spectrometry. *J Phys Chem A*, 110(9):3297–3306, Mar 2006.
- [8] Ales Charvat and Bernd Abel. How to make big molecules fly out of liquid water: applications, features and physics of laser assisted liquid phase dispersion mass spectrometry. *Phys Chem Chem Phys*, 9(26):3335–3360, Jul 2007.

- [9] Zhaoyang Chen, Annemie Bogaerts, and Akos Vertes. Phase explosion in atmospheric pressure infrared laser ablation from water-rich targets. *Applied Physics Letters*, 89(4):041503–041503–3, 2006.
- [10] T. DARDEN, D. YORK, and L. PEDERSEN. Particle mesh ewald - an  $n \cdot \log(n)$  method for ewald sums in large systems. *Journal of Chemical Physics*, 98(12):10089–10092, June 1993.
- [11] X Daura, AE Mark, and WF van Gunsteren. Parametrization of aliphatic chn united atoms of gromos96 force field. *JOURNAL OF COMPUTATIONAL CHEMISTRY*, 19(5):535–547, APR 15 1998. The paper for the GROMOS96 43A1 force field.
- [12] Edward E. Dodd. The statistics of liquid spray and dust electrification by the hopper and laby method. *Journal Of Applied Physics*, 24:73–80, 1953.
- [13] Y Dou. Substrate-assisted laser-initiated ejection of proteins embedded in water films. *The journal of physical chemistry. B*, 107(10):2362–2365, 2003.
- [14] Klaus Dreisewerd. The desorption process in maldi. *Chem Rev*, 103(2):395–426, Feb 2003.
- [15] U. ESSMANN, L. PERERA, M. L. BERKOWITZ, T. DARDEN, H. LEE, and L. G. PEDERSEN. A smooth particle mesh ewald method. *Journal of Chemical Physics*, 103(19):8577–8593, November 1995.
- [16] S Georgiou and F Hillenkamp. Introduction: Laser ablation of molecular substrates. *CHEMICAL REVIEWS*, 103(2):317–319, FEB 2003.
- [17] Savas Georgiou and Antonis Koubenakis. Laser-induced material ejection from model molecular solids and liquids: mechanisms, implications, and applications. *Chem Rev*, 103(2):349–394, Feb 2003.
- [18] B. Hess, H. Bekker, H. J. C. Berendsen, and J. G. E. M. Fraaije. Lincs: A linear constraint solver for molecular simulations. *Journal of Computational Chemistry*, 18(12):1463–1472, September 1997.
- [19] Berk Hess. Convergence of sampling in protein simulations. *Phys Rev E Stat Nonlin Soft Matter Phys*, 65(3 Pt 1):031910, Mar 2002.
- [20] W.F.vanGunsterenand J.Hermans H.J.C.Berendsen, J.P.M.Postma. Interactionmodelsforwaterinrelationtoproteinhydration. *Intermolecular-Forces*, pages 331–342, 1981.

- [21] Jan Hoffmann, Thorsten L Schmidt, Alexander Heckel, and Bernd Brutschy. Probing the limits of liquid droplet laser desorption mass spectrometry in the analysis of oligonucleotides and nucleic acids. *Rapid Commun Mass Spectrom*, 23(14):2176–2180, Jul 2009.
- [22] Holian. Modeling shock-wave deformation via molecular dynamics. *Phys Rev A*, 37(7):2562–2568, Apr 1988.
- [23] Brad Lee Holian, William G. Hoover, Bill Moran, and Galen K. Straub. Shock-wave structure via nonequilibrium molecular dynamics and navier-stokes continuum mechanics. *Phys. Rev. A*, 22(6):2798–2808, Dec 1980.
- [24] W. Kleinekofort, J. Avdiev, and B. Brutschy. A new method of laser desorption mass spectrometry for the study of biological macromolecules. *International Journal of Mass Spectrometry and Ion Processes*, 152(2-3):135 – 142, 1996.
- [25] Richard Knochenmuss and Leonid V Zhigilei. Molecular dynamics model of ultraviolet matrix-assisted laser desorption/ionization including ionization processes. *J Phys Chem B*, 109(48):22947–22957, Dec 2005.
- [26] Andrew R. Leach. *Molecular Modelling: Principles and Applications*. Sharlow, England; New York : Prentice Hall, 2nd edition, 2001. ISBN: 0582382106.
- [27] K Light-Wahl. Observation of the noncovalent quaternary associations of proteins by electrospray-ionization mass-spectrometry. *Journal of the American Chemical Society*, 116(12):5271–5278, 1994.
- [28] Nicholas Metropolis, Arianna W. Rosenbluth, Marshall N. Rosenbluth, Augusta H. Teller, and Edward Teller. Equation of state calculations by fast computing machines. *The Journal of Chemical Physics*, 21(6):1087–1092, 1953.
- [29] S MIYAMOTO and PA KOLLMAN. SETTLE - AN ANALYTICAL VERSION OF THE SHAKE AND RATTLE ALGORITHM FOR RIGID WATER MODELS. *JOURNAL OF COMPUTATIONAL CHEMISTRY*, 13(8):952–962, OCT 1992.
- [30] H. M. Mott-Smith. The solution of the boltzmann equation for a shock wave. *Phys. Rev.*, 82(6):885–892, Jun 1951.

- [31] Chris Oostenbrink, Alessandra Villa, Alan E Mark, and Wilfred F van Gunsteren. A biomolecular force field based on the free enthalpy of hydration and solvation: the gromos force-field parameter sets 53a5 and 53a6. *J Comput Chem*, 25(13):1656–1676, Oct 2004. The paper for the GROMOS96 53A5 53A6 force field.
- [32] Sam-Yong Park, Takeshi Yokoyama, Naoya Shibayama, Yoshitsugu Shiro, and Jeremy R H Tame. 1.25 Å resolution crystal structures of human haemoglobin in the oxy, deoxy and carbonmonoxy forms. *J Mol Biol*, 360(3):690–701, Jul 2006.
- [33] David Van Der Spoel, Erik Lindahl, Berk Hess, Gerrit Groenhof, Alan E Mark, and Herman J C Berendsen. Gromacs: fast, flexible, and free. *J Comput Chem*, 26(16):1701–1718, Dec 2005.
- [34] Wilfred F. van Gunsteren and Herman J. C. Berendsen. Computer simulation of molecular dynamics: Methodology, applications, and perspectives in chemistry. *Angewandte Chemie International Edition in English*, 29(9):992–1023, 1990.
- [35] L Verlet. Computer experiments on classical fluids .i. thermodynamical properties of lennard-jones molecules. *Physical review*, 159(1):98, 1967.
- [36] A. Wattenberg, F. Sobott, and B. Brutschy. Detection of intact hemoglobin from aqueous solution with laser desorption mass spectrometry. *Rapid Commun Mass Spectrom*, 14(10):859–861, 2000.
- [37] Leonid V Zhigilei, Elodie Leveugle, Barbara J Garrison, Yaroslava G Yingling, and Michael I Zeifman. Computer simulations of laser ablation of molecular substrates. *Chem Rev*, 103(2):321–348, Feb 2003.